



FA9550-06-1-0497-FR--2010/01  
Final Report

# III-Nitride Based Optoelectronics

---

## Final Report

**Contract No:** FA9550-06-1-0497

**Period of Performance:** August 2006 – December 2009

**Program Manager:** Dr. Donald Silversmith (AFOSR)

**Principal Investigator:** Professor Manijeh Razeghi

**Institution:** Center for Quantum Devices

Electrical Engineering and Computer Science Department

Northwestern University

2220 Campus Drive: Cook Hall Rm. 4051; Evanston, IL 60208

Tel: (847) 491-7251, Fax: (847) 467-1817

Email: razeghi@eecs.northwestern.edu

**DISCLAIMER.** The views, opinions, and findings contained in this report are those of the author(s) and should not be construed as an official Department of Defense position, policy, or decision, unless so designated by other official documentation.

## REPORT DOCUMENTATION PAGE

Public Reporting burden for this collection of information is estimated to average 1 hour per response, including the time for reviewing instructions, searching existing data sources, gathering and maintaining the data needed, and completing and reviewing the collection of information. Send comment regarding this burden estimates or any other aspect of this collection of information, including suggestions for reducing this burden, to Washington Headquarters Services, Directorate for Information Operations and Reports, 1215 Jefferson Davis Highway, Suite 1204, Arlington, VA 22202-4302, and to the Office of Management and Budget, Paperwork Reduction Project (0704-0188), Washington, DC 20503.

1. AGENCY USE ONLY (Leave Blank)	2. REPORT DATE 03/2010	3. REPORT TYPE AND DATES COVERED Final Technical Report 08/2006-12/2009	
4. TITLE AND SUBTITLE  Deep Ultraviolet Laser Diodes Based on AlGaN Nanostructures		5. FUNDING NUMBERS FA9550-06-1-0497	
6. AUTHOR(S) M. Razeghi			
7. PERFORMING ORGANIZATION NAME(S) AND ADDRESS(ES) Northwestern University Center for Quantum Devices 2220 Campus Drive, Room 4051 Evanston, IL 60208		8. PERFORMING ORGANIZATION REPORT NUMBER 610-4741000-60013281 (S449)	
9. SPONSORING / MONITORING AGENCY NAME(S) AND ADDRESS(ES) U.S. Air Force Office of Scientific Research NE 875 N. Randolph Street Arlington, VA 22203-1954		10. SPONSORING / MONITORING AGENCY REPORT NUMBER	
11. SUPPLEMENTARY NOTES The views, opinions and/or findings contained in this report are those of the author(s) and should not be construed as an official Department of the Air Force position, policy or decision, unless so designated by other documentation.			
12 a. DISTRIBUTION / AVAILABILITY STATEMENT  Approved for public release; distribution unlimited.		12 b. DISTRIBUTION CODE	
13. ABSTRACT (Maximum 200 words)  III-Nitride based optoelectronics support a variety of promising applications due to their tunable direct bandgap extending from deep ultraviolet towards green. We started by studying blue and green light emitting diode (LED) structures based on InGaN/GaN multiquantum wells (MQWs), grown on regular and lateral epitaxial overgrowth (LEO) GaN templates. We apply a unique pulsed epitaxy approach to achieve green LEDs. We also studied InGaN quantum dots for improved emission in the green spectrum.  A novel hybrid green light-emitting diodes (LEDs) comprised of <i>n</i> -ZnO/ (InGaN/GaN) multi-quantum-wells/ <i>p</i> -GaN were developed. The low temperature pulsed laser deposition (PLD) of the ZnO avoids the degradation typical when capping structures via metalorganic chemical vapor deposition. The results indicate that hybrid LED structures hold the prospects for development green LEDs with superior performance.  We also report on the current-voltage characteristic under forward biases obtained in low leakage, small size <i>p</i> -(In,Ga)N/GaN- <i>n</i> multiquantum well diodes. The detection of very low photon fluxes was reported under gated biasing in the 1 MV/cm range. We also reported on the fabrication and current-voltage characteristics of nanostructured p-i-n photodiodes based on GaN. Strong rectifying behavior was obtained; In contrast to GaN bulk p-i-n diodes, devices reproducibly show ideality factors lower than 2.			
14. SUBJECT TERMS  III-Nitrides, GaN, InGaN, Green, Blue, LEDs, optoelectronics, ultraviolet, photodetectors		15. NUMBER OF PAGES 60	
		16. PRICE CODE	
17. SECURITY CLASSIFICATION OR REPORT UNCLASSIFIED	18. SECURITY CLASSIFICATION ON THIS PAGE UNCLASSIFIED	19. SECURITY CLASSIFICATION OF ABSTRACT UNCLASSIFIED	20. LIMITATION OF ABSTRACT UL

NSN 7540-01-280-5500

Standard Form 298 (Rev.2-89)  
described by ANSI Std. Z39-18  
98-102

20100504285

## Table of Contents

<b>1</b>	<b>Introduction.....</b>	<b>1</b>
<b>2</b>	<b>Blue and green multi-quantum-well LEDs grown on conventional and lateral epitaxial overgrowth GaN .....</b>	<b>2</b>
2.1	Introduction.....	2
2.2	Experiment.....	3
2.2.1	Growth and Material Characterization.....	3
2.2.2	Preparation of high quality LEO GaN .....	3
2.2.3	Blue and green active layers on conventional and LEO GaN .....	7
2.2.4	Fabrication of blue and green LEDs on conventional and LEO GaN.....	9
2.3	Device Results and Discussions.....	9
2.4	Conclusion .....	13
<b>3</b>	<b>Green Light Emitting Diodes.....</b>	<b>14</b>
3.1	Introduction.....	14
3.2	Experiment.....	15
3.3	Result and Discussion.....	17
3.4	Conclusion .....	18
<b>4</b>	<b>InGaN Quantum Dots for Green Emission .....</b>	<b>18</b>
4.1	Introduction.....	18
4.2	Experiment.....	18
4.3	Result and Discussion.....	18
<b>5</b>	<b>Novel Inverted Hybrid Green LEDs Based on <i>n</i>-type ZnO and InGaN MQWs</b>	<b>25</b>
5.1	Introduction.....	25
5.2	Experiment.....	25
5.3	Results and Discussion .....	26
5.3.1	Structural characterization of the layers.....	26
5.3.2	Electrical characterization of the layers .....	27
5.3.3	Optical characterization of the layers.....	28
5.3.4	Effect of common solvents on ZnO .....	29
5.3.5	Effect of annealing .....	30
5.3.6	Etching Study.....	30
5.3.7	Device Performance.....	31
5.4	Summary .....	33
<b>6</b>	<b>High Optical Response in Forward Biased InGaN–GaN Multiquantum-Well Diodes Under Barrier Illumination.....</b>	<b>33</b>
6.1	Introduction.....	33
6.2	Sample growth and device fabrication.....	34
6.3	Results and Discussion .....	34
6.3.1	Electro-optical characteristics .....	34
6.3.2	Band diagram .....	38
6.3.3	Barrier electric field .....	40
6.4	Model and I-V curve analysis .....	43
6.5	Detection of low photon fluxes.....	46
6.6	Summary .....	47
<b>7</b>	<b>GaN Nanostructured <i>p-i-n</i> Photodiodes.....</b>	<b>47</b>
7.1	Introduction.....	47

7.2	Material Growth & Processing .....	48
7.3	Results and Analysis .....	49
7.4	Summary .....	52
<b>8</b>	<b>Conclusions.....</b>	<b>52</b>
<b>9</b>	<b>References.....</b>	<b>53</b>

## 1 Introduction

III-Nitrides, long regarded as a scientific curiosity, have now earned a most respectful place in the science and technology of compound semiconductors and optoelectronic devices. III-Nitrides cover a wide spectral range from UV to the IR and have the potential to be utilized in numerous different optoelectronic devices. In this report we discuss novel III-Nitride based optoelectronic devices including: blue & green LEDs on LEO and conventional substrates, InGaN quantum dot based LEDs, hybrid ZnO-InGaN based green LEDs, multi-quantum well detectors that show internal gain, and nano-structured UV detectors with improved electrical properties.

In section 2 “*Blue and green multi-quantum-well LEDs grown on conventional and lateral epitaxial overgrowth GaN*”, growth of blue and green multi-quantum-wells (MQWs) and light-emitting diodes (LEDs) are realized on lateral epitaxial overgrowth (LEO) GaN, and compared with identical structures grown on conventional GaN. Atomic force microscopy is used to confirm the significant reduction of dislocations in the wing region of our LEO samples before active region growth. Differences between surface morphologies of blue and green MQWs are analyzed. These MQWs are integrated into LEDs. All devices show a blue shift in electroluminescence (EL) peak, and narrowing in EL spectra with increasing injection current, both characteristics attributed to the bandgap renormalization. Green LEDs show a larger EL peak shift and broader EL spectrum due to larger piezoelectric field and more indium segregation in the MQWs, respectively. Blue LEDs on LEO GaN show a higher performance than those on conventional GaN, however, no performance difference is observed for green LEDs on LEO GaN versus conventional GaN. The performance of the green LEDs is shown to be primarily limited by the active layer growth quality.

Increasing the In content of the active layer, an apparent decrease in the intensity is observed. In section 3 “*Green Light Emitting Diodes*”, we identify the problem, and apply our unique pulsed epitaxy approach to achieve green LEDs.

In Section 4 “*InGaN Quantum Dots for Green Emission*”, the growth and optical properties of self-assembled InGaN quantum dots (QDs) on GaN templates are reported. The effects of growth temperature, deposition thickness and V/III ratio on QD formation are examined. The critical thickness for QD formation of  $\text{In}_{0.54}\text{Ga}_{0.46}\text{N}$  on GaN is experimentally determined to be 3.3 monolayers (ML). Room temperature photoluminescence at 558 nm with a full width at half maximum of 117 meV is achieved from the InGaN QDs. Compared with InGaN quantum wells (QWs), InGaN QDs present a narrower emission at 558 nm. The capping of QDs with low temperature GaN is analyzed. Our work demonstrates high optical quality InGaN quantum dots emitting in green spectrum can be realized by optimizing the growth parameters.

In section 5 “*Novel Inverted Hybrid Green LEDs Based on n-type ZnO*”, we demonstrate our unique approach for green light emitting diodes. Although ultra-bright and efficient blue InGaN-based Light Emitting Diodes (LEDs) are readily available, the performance of InGaN-based green LEDs is still relatively poor. This is because the higher In content required in the active layers for green emission causes problems. In particular, the elevated substrate temperature ( $T_s$ ) necessary for the *p*-type GaN top layer causes In to leak out of the active layers in the InGaN/GaN Multi-Quantum Wells

(MQW). This significantly reduces the performance and lifetime of the LEDs. In this work, an *n*-type ZnO was substituted for the *n*-type GaN layer in an (In)GaN-based green LED with an inverted *p-n* structure. The top layer was thus the *n*-type ZnO rather than *p*-type GaN. Through use of Pulsed Laser Deposition (PLD) for this ZnO growth, the ultimate growth step could thus be performed at significantly lower  $T_s$  than is typically required for GaN growth in Metal-Organic Chemical Vapor Deposition (MOCVD). High crystallographic quality of the final hybrid LED structure and the integrity of the MQWs were confirmed by x-Ray Diffraction. The devices showed rectifying I-V characteristics with a turn-on voltage of 2.5 V and a discrete green Electroluminescence (EL) emission peaked at around 510 nm, which was readily visible to the naked eye. These results indicate that PLD-grown ZnO could be a good alternative to MOCVD-grown GaN for the *n*-type layer and that such inverted hybrid structures could hold the prospect for the development of green LEDs with superior performance.

In section 6, “*High Optical Response in Forward Biased InGaN–GaN Multiquantum-Well Diodes Under Barrier Illumination*” we discuss a novel multi-quantum well device structure. Under barrier illumination, the devices present a high optical response with capabilities to detect optical powers in the pW range without further amplification. By modeling the device operation we can get a better understanding for the origins of this behavior. Due to their high internal gain, these devices present the interesting opportunity to be used for the detection of low photon fluxes.

In section 7, “*GaN Nanostructured *p-i-n* Photodiodes*” we discuss a novel approach to the realization of GaN based UV photodetectors. Each device comprises arrays of 1  $\mu\text{m}$  separated nanopillars fabricated by e-beam lithography with diameters of  $\sim 200$  nm. In contrast to conventional bulk GaN *p-i-n* diodes, devices these nano-structured devices have the ability to show ideality factors of less than 2.

## 2 Blue and green multi-quantum-well LEDs grown on conventional and lateral epitaxial overgrowth GaN

### 2.1 Introduction

Solid state lighting (SSL) holds the promise of a more energy-efficient, longer-lasting, more compact, and lower maintenance substitute for today's incandescent and fluorescent light sources. Since lighting currently represents about 22% of all electricity consumption, the adoption of SSL could significantly reduce greenhouse gas emissions.<sup>1</sup> Light-emitting diodes (LEDs) based on  $\text{In}_x\text{Ga}_{1-x}\text{N}$  alloys, are currently the most promising candidates for realizing efficient SSL. InGaN is a direct wide bandgap semiconductor with an emission which can span the entire visible spectrum via compositional tuning. However, InGaN LED performance is highly wavelength-dependent. Indeed, ultra-bright and efficient blue InGaN-based LEDs are readily available<sup>2</sup> but the efficiency of InGaN-based green LEDs is still far from adequate for use in SSL.<sup>3,4,5</sup>

The lack of economical lattice-matched substrates for the growth of III-Nitrides necessitates the usage of GaN-mismatched silicon carbide (SiC) or sapphire ( $\text{Al}_2\text{O}_3$ ) substrates, which leads to dislocation densities on the order of  $10^8 \text{ cm}^{-2}$ . The high performance of blue LEDs in spite of these dislocations is attributed to indium

segregation in the InGaN layers that produces nanometer-wide indium-rich regions that behave like quantum dots.<sup>6,7</sup> These quantum dots (QDs) localize the carriers, and prevent them from recombining non-radiatively at the dislocation sites.<sup>8,9</sup> Difficulty in realizing high power green LEDs has three major parts (1) the limited solubility of indium in InGaN<sup>10</sup> imposes a restricted growth window for the green-emitting InGaN active layer, (2) InGaN with high indium content becomes unstable at elevated growth temperatures required for other layers in the device<sup>11</sup> leading to indium migrating out of the active layers, which reduces the LED spectral quality,<sup>5,11</sup> (3) InGaN with high indium content generates dislocations leading to lower performance.<sup>12</sup>

Blue and green LEDs grown on conventional GaN have been compared in order to study the wavelength-dependent device performance.<sup>13,14,15</sup> Blue LEDs and laser diodes (LDs) grown on LEO GaN have also been studied in other works, showing superior performance to those grown on conventional GaN.<sup>16,17</sup> Devices on LEO GaN offer lower leakage current,<sup>16,18,19</sup> higher stability, better thermal properties,<sup>17</sup> and longer device lifetime.<sup>20</sup> Despite these advantages, there are no studies of green active layers and LEDs on LEO GaN. In this work, we analyze blue and green active layers on conventional and high quality LEO GaN by x-ray diffraction (XRD), atomic force microscopy (AFM) and photoluminescence (PL). Then, we integrate them into LEDs, compare and correlate the material characteristics and device performance.<sup>21</sup>

## 2.2 Experiment

### 2.2.1 Growth and Material Characterization

MQWs and LEDs were grown on double side polished *c*-plane sapphire substrate in an Aixtron 200/4-HT, horizontal flow, low pressure, metal organic chemical vapor deposition (MOCVD) reactor. Trimethylaluminum (TMAl), Trimethylgallium (TMGa), and Trimethylindium (TMIn) were the metalorganic cation precursors for Al, Ga, and In sources, respectively. Bis(cyclopentadienyl)magnesium ( $Cp_2Mg$ ) and Silane ( $SiH_4$ ) were used as the *p*- and *n*-type doping sources, respectively. Ammonia ( $NH_3$ ) was used as the nitrogen anion source. Nitrogen was used as the carrier gas for growth of the MQWs to help increase indium incorporation whereas hydrogen was used during the rest of the layers.

### 2.2.2 Preparation of high quality LEO GaN

Growth began with desorption of the sapphire substrate at 1100 °C under  $H_2$ . Then, a thin low-temperature GaN buffer layer was grown, followed by 2  $\mu m$  of GaN, grown at 1050 °C. In order to create a mask for lateral overgrowth, the wafer was removed from the reactor and 50 nm of silicon nitride ( $Si_3N_4$ ) was deposited by plasma enhanced chemical vapor phase deposition (PECVD) and patterned along the  $GaN <1\bar{1}00>$  direction with openings of 2  $\mu m$  and a period of 15  $\mu m$ .<sup>22</sup> This pattern direction exposes the A-planes ( $11\bar{2}0$ ) for lateral growth and is known to give fastest lateral growth rate and high quality wing regions.<sup>23</sup> For higher device performance, smaller fill factors (ratio of mask opening width to stripe period) are desired, which makes regrowth more challenging.<sup>24</sup> We have used a fill factor of 0.13 to have a larger wing area and to perform better analysis.

Etching of the opening in the  $\text{Si}_3\text{N}_4$  layer was performed by electron cyclotron resonance reactive ion etching (ECR-RIE) using an  $\text{SF}_6$  based chemistry; we have observed that this ECR-RIE chemistry does not etch GaN appreciably, however, some surface damage is observed by scanning electron microscope (SEM). Some  $\text{Si}_3\text{N}_4$  residuals were observed on the GaN opening regions via AFM. However, when GaN regrowth tests were conducted in these opening regions, a smooth GaN surface was observed via SEM, showing that slight remaining  $\text{Si}_3\text{N}_4$  residues did not have a detrimental effect on the GaN regrowth. Proper trade-off must be made between etching time and surface damage, and amount of  $\text{Si}_3\text{N}_4$  residual atoms in the GaN opening in correlation with the regrowth characteristics.

After etching, samples were cleaned with trichloroethylene, acetone, methanol, and rinsed thoroughly. Then, samples were placed inside the reactor for our optimized five-step LEO GaN re-growth. A cross-sectional sketch of the LEO GaN steps is shown in Figure 1.

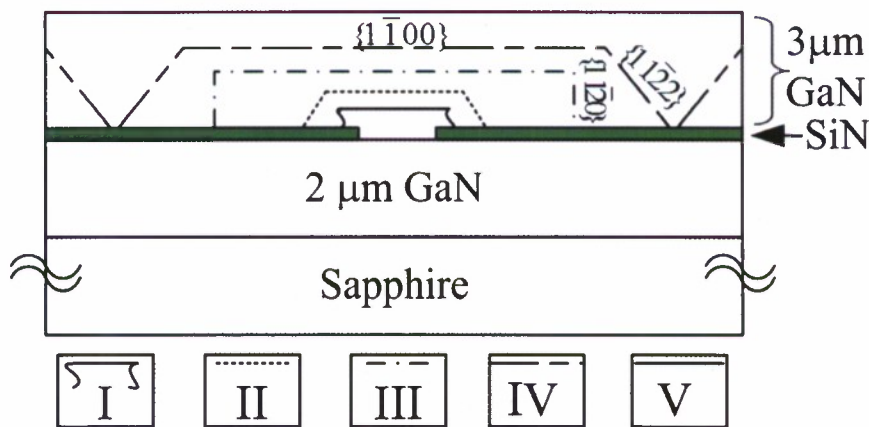


Figure 1. Schematic sketch of our optimized five-step LEO GaN growth process.

**Step I** is designed for high surface diffusion to minimize nucleation on the SiN mask and promote vertical growth on the GaN in the  $\text{Si}_3\text{N}_4$  openings in order to create an initial well-formed seed from which the vertical growth will progress. The vertical thickness should be around double the  $\text{Si}_3\text{N}_4$  layer thickness. Important growth parameters such as growth temperature, V/III ratio, effective lateral to vertical growth rate ratio, and growth time are given in Table 1.

**Step II** is similar to **Step I** except the growth conditions are adjusted to favor both lateral and vertical growth in order to obtain straight side walls.<sup>25</sup> Growth temperature is increased and V/III ratio is decreased, as given in Table 1. If Ga and N adatoms are too mobile, then they tend to align themselves exactly as the etching pattern. However, since the edges of the  $\text{Si}_3\text{N}_4$  mask are not perfectly straight lines, this step is needed to achieve better straight sidewalls. At the end of this step well formed inclined  $\{11\bar{2}2\}$  facets are observed.

**Step III** is the lateral growth phase, during which the lateral to vertical (L/V) growth rate is enhanced by increasing the growth temperature.<sup>24</sup> Increasing effective lateral to vertical growth rate ratio (L/V) decreases the growth time required for coalescence, and helps bend the threading dislocations sideways.<sup>23</sup> During the first part of **Step III** the

initially inclined  $\{11\bar{2}2\}$  sidewalls begin to tilt, and are replaced with vertical  $\{11\bar{2}0\}$  sidewalls (Figure 1). This change in the growth direction over the first three steps, from vertical to lateral, helps to bend the threading dislocations sideways so that they do not propagate to the surface.

**Step IV** is the coalescence step; after the distance between the side walls is close enough, the side wall slope is increased, as shown in Figure 1 in order to realize a void free coalescence front. This is achieved by decreasing the growth temperature sufficiently so that growth favors the formation of inclined  $\{11\bar{2}2\}$  facets.<sup>24</sup> This inclination minimizes the voids and prevents the dislocations spreading at the coalescence front. Failure to control the lateral to vertical growth rate during coalescence results in the formation of voids and leads the LEO GaN surface to bend, both can be observed by SEM. During this phase, the lower temperature necessary to realize inclined planes results in less surface diffusion, and the lack of exposed  $\text{Si}_3\text{N}_4$  removes the supply of excess adatoms at the facet edge.<sup>26</sup> This results in a slow lateral growth rate, requiring a longer time for full coalescence.

**Step V** is similar to conventional GaN growth and promotes vertical growth. *n*-type doping is achieved by introducing  $\text{SiH}_4$  during this step, as LEDs will be grown on this template. Typically up to 0.6  $\mu\text{m}$  is grown in this layer. The GaN vertical growth height at full coalescence is  $\sim 5 \mu\text{m}$ , small enough that wafer bending effects are minimal.<sup>27</sup>

LEO Step:	$T_{\text{growth}}(\text{°C})$	V/III Ratio	L/V Ratio	$t_{\text{growth}}$ (mins)
<b>Step I</b>	1080	6000	1.1	4
<b>Step II</b>	1100	2930	2.4	60
<b>Step III</b>	1130	2930	2.6	60
<b>Step IV</b>	1100	2930	1.4	195
<b>Step V</b>	1040	2400	1.0	30

*Table 1. Important growth parameters for LEO GaN (2  $\mu\text{m}$  opening 15  $\mu\text{m}$  period): LEO Step number, growth temperature ( $T_{\text{growth}}(\text{°C})$ ), V/III ratio, effective lateral to vertical growth rate ratio (L/V), and growth time ( $t_{\text{growth}}$ ).*

Table 1 summarizes the basic growth parameters for the above explained five-step LEO growth process (Figure 1) for an opening of 2  $\mu\text{m}$  and period of 15  $\mu\text{m}$ . It should be possible to reach high quality LEO GaN for different filling factors and periods, by employing the ideas described in each growth step.

Figure 2 displays the AFM of the fully coalesced LEO GaN templates. The surface above the opening region (Figure 2(a)), is similar to that of conventional GaN, exhibiting chaotic atomic steps, the surface termination of which identify screw/mixed type threading dislocations.<sup>26</sup> Contrarily, the wing region (Figure 2(b)), where lateral growth occurs, possesses well ordered parallel atomic steps with no atomic step terminations. The entire surface, including the coalescence region, where the neighboring atomic steps interfere, is observed in Figure 2(c). In order to study the dislocations, a hot (170  $^{\circ}\text{C}$ )

phosphoric acid (85%  $\text{H}_3\text{PO}_4$ ) treatment for 15 minutes was used.<sup>19,28</sup> This etch-pit-density study reveals no discernable dislocations in the wing areas, whereas in the LEO GaN coalescence area, and opening region dislocation densities of  $(2\pm1)\times 10^8 \text{ cm}^{-2}$ , and  $(9\pm2)\times 10^8 \text{ cm}^{-2}$  are observed, respectively (Figure 2(d)). For comparison, conventional GaN was observed to have a dislocation density of  $(9\pm1)\times 10^8 \text{ cm}^{-2}$ . This phosphoric acid treatment is capable of distinguishing between edge and screw or mixed type dislocations.<sup>19,28</sup> The bigger pits correspond to dislocations with screw component whereas smaller ones correspond to edge type dislocations. It is known that edge type dislocation may exist in the wing region as their bending is very sensitive to growth conditions.<sup>29</sup> The non-existence of any discernable dislocations on our wing regions show the quality of the five-step LEO GaN developed, and establish a baseline from which we can study the effect of dislocations on blue and green InGaN based LEDs. For LEO GaN, no GaN peak separation is observed (in Figure 3) which shows that there is no significant plane tilt,<sup>30</sup> supporting our high quality growth scheme described.

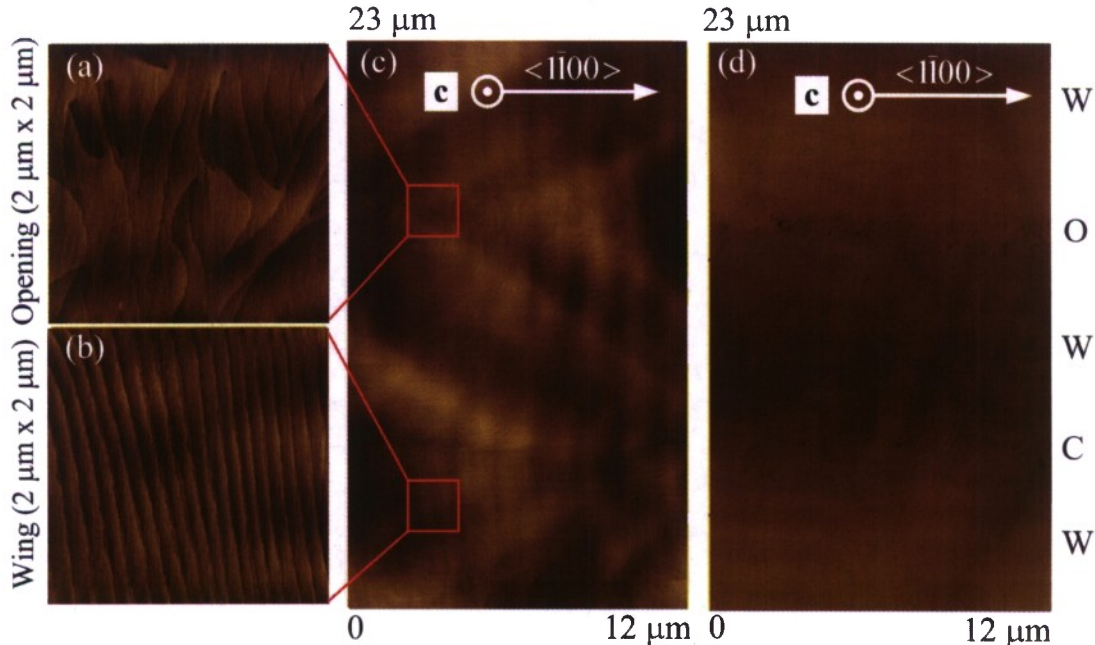


*Figure 2. AFM images of coalesced LEO GaN. (a) opening (2  $\mu\text{m} \times 2 \mu\text{m}$ ) and (b) wing (2  $\mu\text{m} \times 2 \mu\text{m}$ ) have root mean square (RMS) roughness of 1.9  $\text{\AA}$  and 1.5  $\text{\AA}$ , respectively. (c) displays larger area (12  $\mu\text{m} \times 23 \mu\text{m}$ ) AFM scan. (d) displays dislocations, revealed by hot phosphoric acid treatment, which are seen as dark spots. 'W', 'O' and 'C' corresponds to wing, opening and coalescence regions, respectively.*

After preparation of LEO templates as described above, blue and green MQWs and LEDs are grown simultaneously on these templates, and on conventional GaN for comparison purposes. Each quantum well was composed of 3.5 nm thick InGaN with a 7.0 nm thick GaN barrier. The thicknesses of the blue and green MQW layers are arranged to be the same in order to have a better comparison. Growth temperatures of the MQWs are adjusted to ensure blue and green luminescence from the InGaN QWs. These MQWs were capped with 550 nm thick *p*-GaN complete the LED structure.

### 2.2.3 Blue and green active layers on conventional and LEO GaN

Open detector x-ray diffraction (XRD) studies and XRD simulations are carried out to confirm the indium composition, and InGaN and GaN thicknesses of the active layer. Figure 3 displays the (0002) XRD ( $\omega/2\Theta$ ) scan for blue and green three-MQWs on LEO and conventional GaN. The XRD simulations of these MQWs are also plotted, and show good agreement with the experimental data. The InGaN and GaN thicknesses are determined as 3.5 and 7.0 nm, respectively. The indium content in the InGaN well is calculated to be 20% for blue MQWs and 28% for green MQWs. The 0<sup>th</sup> order MQW peak is more distinctly observed in green MQWs due to higher average indium content in these structures.

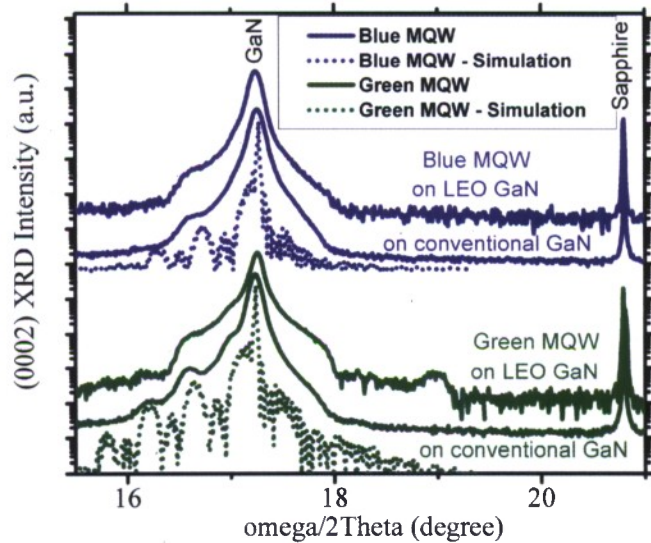


**Figure 3.** (0002) XRD  $\omega/2\Theta$  scan of blue and green MQWs on conventional and LEO GaN. The XRD simulation is realized to compare with experimental results.

Atomic force microscopy is used to study the surface morphology of the MQW active layers. Figure 4 shows the AFM images of the last barrier of blue MQWs on LEO and conventional GaN. Screw type threading dislocations are observed to be dominant on the opening (Figure 4(a)). Figure 4(b,c) show that active layer on wing area has much fewer dislocations and a much smoother surface than that on conventional GaN. This is directly related to the lower dislocation density in the wing area. Figure 5 shows the AFM images of green MQWs on LEO and conventional GaN. Screw type dislocations are still dominant in the opening region. Although less dislocations are observed on the wing than that on the conventional GaN (Figure 5(b,c)), an island-like (2D) growth is observed to be dominant across the LEO stripe, different from the blue active layer case (Figure 4). The lower deposition temperature necessary to realize a green active layer results in an island-like growth rather than a layer-by-layer growth as was observed for blue layer. In summary, the wing regions are observed to be smoother than opening regions.

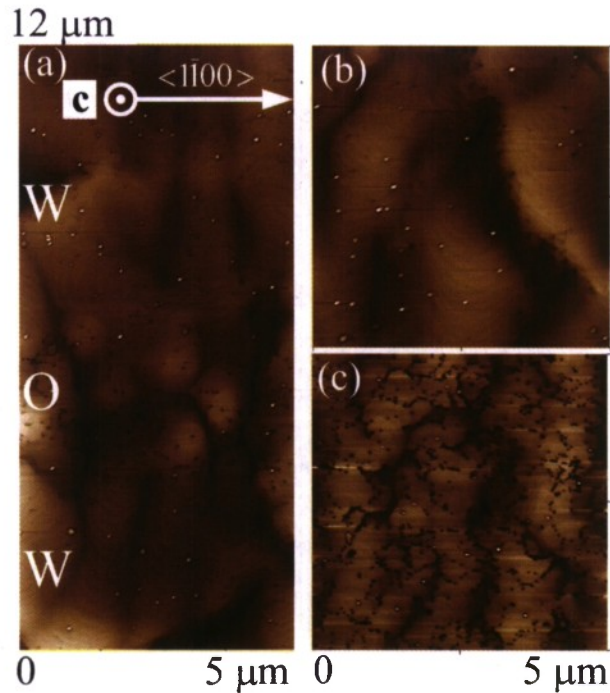


Figure 4. AFM images of blue MQWs on (a) LEO GaN ( $5 \mu\text{m} \times 12 \mu\text{m}$ ), (b) wing area of LEO GaN ( $5 \mu\text{m} \times 5 \mu\text{m}$ ), (c) conventional GaN ( $5 \mu\text{m} \times 5 \mu\text{m}$ ). 'W', and 'O' corresponds to the wing and opening regions, respectively.

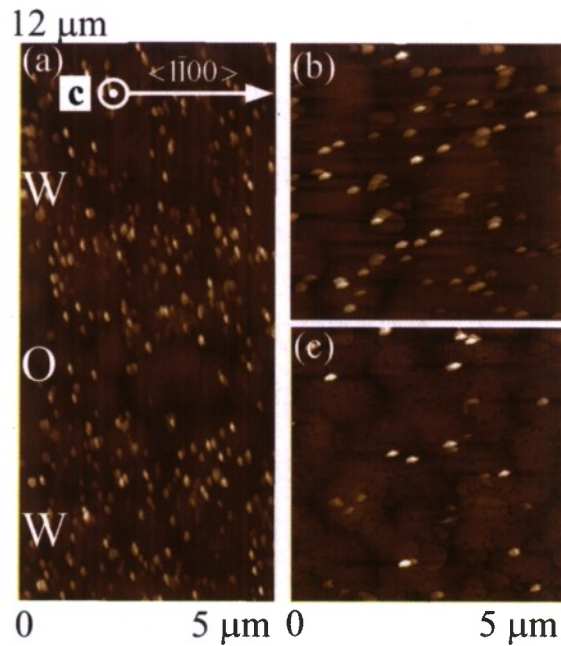


Figure 5. AFM images of green MQWs on (a) LEO GaN ( $5 \mu\text{m} \times 12 \mu\text{m}$ ), (b) wing area of LEO GaN ( $5 \mu\text{m} \times 5 \mu\text{m}$ ), (c) conventional GaN ( $5 \mu\text{m} \times 5 \mu\text{m}$ ). 'W', and 'O' corresponds to the wing and opening regions, respectively.

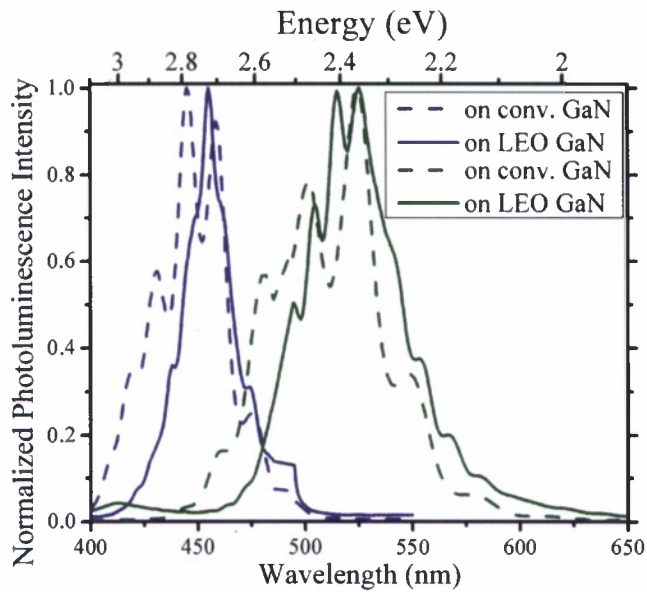


Figure 6. Room temperature PL of blue and green active layers.

Room-temperature (RT) photoluminescence of these blue and green emitting MQWs are shown in Figure 6. The PL wavelength of MQWs on LEO GaN is observed to be slightly higher than that of the same structure grown on conventional GaN. This could be due to increase in *c*-plane lattice constant of LEO GaN,<sup>31</sup> leading to a smaller compositional pulling effect,<sup>32</sup> thus allowing slightly more indium into the InGaN.

#### 2.2.4 Fabrication of blue and green LEDs on conventional and LEO GaN

Blue and green active layers composed of seven-MQWs were grown as described above with the addition of a 550 nm thick *p*-GaN capping layer to complete the LED structure. Activation of the *p*-type GaN is achieved by rapid thermal annealing (RTA) at 1000 °C for 30 s in nitrogen ambient. After this the surface is treated with HCl:H<sub>2</sub>O (1:1), 30 Å Ni/30 Å Au is deposited and annealed for 10 mins under air to achieve a transparent ohmic contact to *p*-GaN. ECR-RIE (SiCl<sub>4</sub>:Ar based chemistry) is used to etch 300 μm × 300 μm mesas, thus, each LED mesa spans many opening, wing, and coalescence regions. Finally, 400 Å Ti/1200 Å Au is deposited as a thick *n*-type contact and to serve as a central bond pad on top of the thin transparent *p*-contact in order to complete the LED fabrication.

### 2.3 Device Results and Discussions

The blue and green LED on conventional GaN are hereinafter referred as “B<sub>Conv.</sub>” and “G<sub>Conv.</sub>” whereas those on LEO GaN as “B<sub>LEO</sub>” and “G<sub>LEO</sub>”, respectively. Figure 7(a, b) show the I-V curves of blue and green LEDs on conventional and LEO GaN. A clear improvement in reverse-bias leakage characteristics is observed between samples B<sub>LEO</sub> and B<sub>Conv.</sub> whereas no significant difference is observed between samples G<sub>Conv.</sub> and G<sub>LEO</sub>.

Reverse bias characteristics of the LEDs are studied in detail. The majority of the leakage current is expected to flow through the LED, with only a small portion

contributed by surface leakage.<sup>33</sup> The leakage current through nitride *p-i-n* devices is known to be dominated by hopping of charged carriers via localized defect-related states (traps) in the depletion region.<sup>34,35</sup> In the case of defect dominated reverse conduction, the reverse I-V characteristics of LEDs can be modeled as:<sup>19</sup>

$$\text{Equation 1} \quad I = I_0 e^{qV/E_0} \quad (1),$$

where  $V$  and  $E_0$  are the diode voltage and the energy parameter, respectively, with  $I_0$  being a pre-exponential factor.  $E_0$  represents the electrical activities of dislocations with a screw component, and is known to be dependent on the voltage at which the fitting is realized.<sup>19,34,35</sup> For electrical fields  $E \ll (2kT/q\alpha) \approx 5 \times 10^5 \text{ V/cm}$  (assuming  $\alpha$ , the localization radius of the electron wave function, is 10 Å), thermionic emission over a barrier dominates the leakage current.<sup>18</sup> We have used the fitting at low voltage range ( $1 < V < 5$ ). In this range,  $I_0$  and  $E_0$  are related to the density and to the electrical activities of dislocations with a screw component, respectively.<sup>19,33,34,35,36</sup> Using Equation 1 to fit the *I-V* curves, reverse bias parameters  $I_0$  and  $E_0$  are calculated, and given in Table 2.

Identifier	Device	$I_0$ ( $\mu\text{A}$ )	$E_0$ (eV)
$B_{\text{Conv.}}$	Blue LED on conventional GaN	$7.86 \times 10^{-6}$	1.34
$B_{\text{LEO}}$	Blue LED on LEO GaN	$3.17 \times 10^{-10}$	0.73
$G_{\text{Conv.}}$	Green LED on conventional GaN	$2.01 \times 10^{-6}$	0.91
$G_{\text{LEO}}$	Green LED on LEO GaN	$2.16 \times 10^{-6}$	0.80

Table 2. Important calculated/fitted LED parameters: leakage current pre-exponential factor ( $I_0$ ), electrical activities of dislocations with a screw component factor ( $E_0$ ).

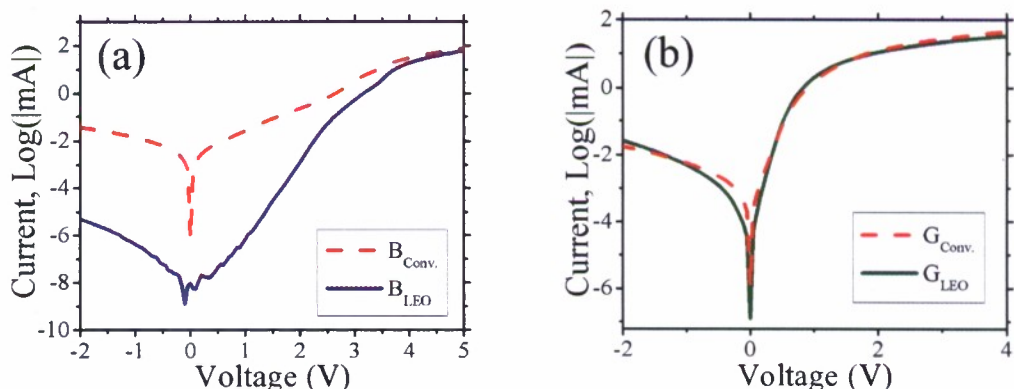
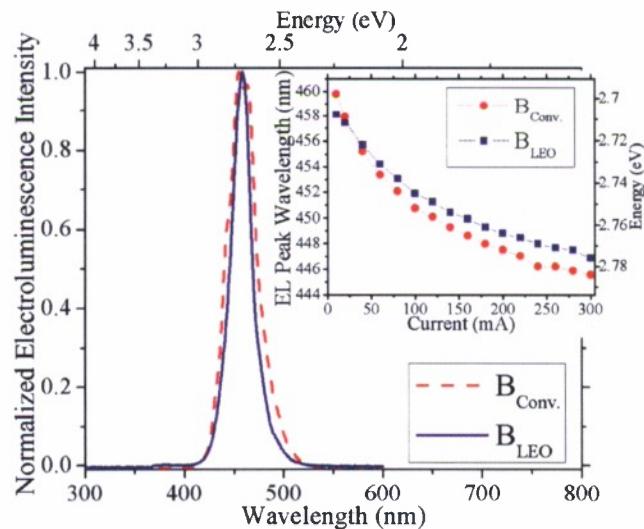


Figure 7. Current-Voltage curves (logarithmic scale) of blue and green LEDs on conventional ( $B_{\text{Conv.}}, G_{\text{Conv.}}$ ) and LEO GaN ( $B_{\text{LEO}}, G_{\text{LEO}}$ ).

$I_0$  is related to square of the density of dislocations with a screw component.<sup>19</sup> Comparing  $I_0$  values among the different samples in Table 2 suggests  $B_{\text{LEO}}$  has approximately two orders of magnitude lower dislocation density than  $B_{\text{Conv.}}$ . This agrees with the etch-pit-density study of the LEO GaN (Figure 2). For  $G_{\text{Conv.}}$  and  $G_{\text{LEO}}$ , no significant difference in  $I_0$  is observed. As the same LEO GaN templates are used for  $B_{\text{LEO}}$  and  $G_{\text{LEO}}$ , the active layer used in samples  $G_{\text{Conv.}}$  and  $G_{\text{LEO}}$  is the dominant dislocation generator leading to uniform dislocation distribution through the active layer. This helps explaining why we do not see a significant difference in  $I_0$  between samples  $B_{\text{Conv.}}$ ,  $G_{\text{Conv.}}$ , and  $G_{\text{LEO}}$ .

$E_0$  is very sensitive to the growth conditions,<sup>19</sup> thus blue ( $B_{\text{Conv.}}$  and  $B_{\text{LEO}}$ ), and green ( $G_{\text{Conv.}}$  and  $G_{\text{LEO}}$ ) emitters should be considered separately. The lower value for sample  $B_{\text{LEO}}$  compared to  $B_{\text{Conv.}}$  could be due to periodic alignment of the dislocations leading to a stronger voltage dependency of leakage current. A similar trend is observed between  $G_{\text{LEO}}$  and  $G_{\text{Conv.}}$ ; however, it is less pronounced, due to the generation of additional dislocations in the active layer creating an almost homogeneous dislocation density similar to conventional GaN (Figure 4 & Figure 5). The higher active layer quality of sample  $B_{\text{Conv.}}$  compared to  $G_{\text{Conv.}}$  could be the reason for higher value of  $E_0$  leading to smaller dependency of leakage current on voltage.



**Figure 8. Electroluminescence spectra of blue LED on conventional (B<sub>Conv.</sub>) and LEO GaN (BLEO) under 20 mA current injection. Inset displays the peak wavelength at different current injections.**

Electroluminescence (EL) spectra were acquired for the LEDs under pulsed current injection (duty cycle of 10% and frequency of 5 kHz) in order to help reduce heating effects under higher current injection (Figure 8 & Figure 9). The minimal role heating was confirmed by measuring the peak intensity versus power and noting that, for the currents used in this study, no thermal roll-over was observed to occur. The EL spectra of blue LEDs are shown in Figure 8. The inset shows that both devices demonstrate a blue shift (from 465 to 446 nm) with increasing current. The decrease in wavelength with injection current is attributed to bandgap renormalization (due to free carrier screening of the piezoelectric (PE) field). At all but the lowest currents,  $B_{\text{LEO}}$  has a slightly longer

wavelength emission than  $B_{\text{Conv.}}$  (Figure 8 inset). In previous blue LED studies, a similar observation has been reported.<sup>16</sup> This observation is in agreement with the PL that was discussed in section 2.2.3. Device  $B_{\text{LEO}}$  has a narrower EL spectra than  $B_{\text{Conv.}}$  (Figure 10). This suggests a more uniform indium distribution throughout the active layer.<sup>7</sup> Indeed, Figure 4 directly illustrates the more uniform surface of blue MQWs on LEO GaN, supporting the advantage of LEO templates.

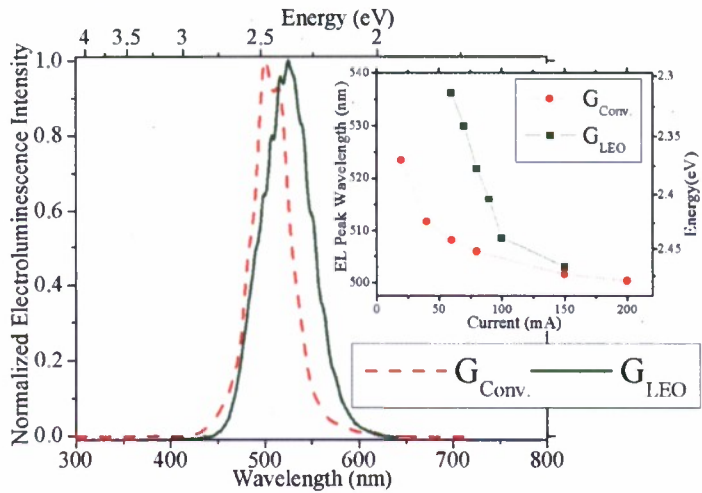


Figure 9. Electroluminescence spectra of green LED on conventional ( $G_{\text{Conv.}}$ ) and LEO GaN ( $G_{\text{LEO}}$ ) under 80 mA current injection. Inset displays the peak wavelength at different current injections.

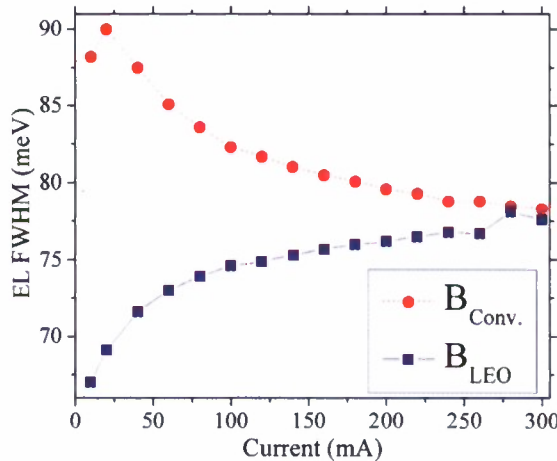
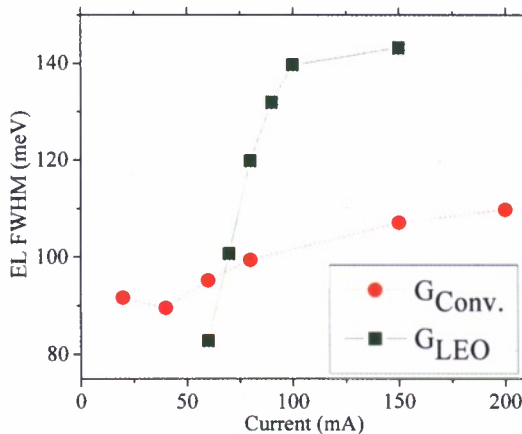


Figure 10. EL FWHM dependency on current for blue LED on conventional ( $B_{\text{Conv.}}$ ) and LEO GaN ( $B_{\text{LEO}}$ ).

In Figure 10 the EL FWHMs of the blue LEDs are plotted as a function of the injection current; the FWHM of device on conventional GaN can be seen to decrease with current, while the FWHM of the device on LEO GaN can be seen to increase. The EL FWHM broadening in  $B_{\text{LEO}}$  could be related to dislocation alignment in the LEO openings resulting in an electric field built up.



**Figure 11.** EL FWHM dependency on current for green LED on conventional (GConv.) and LEO GaN (GLEO).

The EL spectra of the green LEDs are shown in Figure 9. Device G<sub>LEO</sub> is observed to have longer peak wavelength than device G<sub>Conv.</sub> (Figure 9 inset). With increasing current, the EL FWHM increased for both devices (Figure 10); however, the EL peak-shift of sample G<sub>LEO</sub> is larger than that of G<sub>LEO</sub>, possibly due to the effects of piezoelectric fields. These piezoelectric fields may also be responsible for the broader EL FWHM observed in green LEDs. (This could be seen by comparing the ordinates of Figure 10 and Figure 11)

Comparing blue and green LEDs, a more pronounced EL peak shift is observed for green LEDs. This suggests stronger piezoelectric effects in the active layer. Piezoelectric effects are expected to be more pronounced in green MQWs due to the higher indium content of the layers.<sup>14</sup> The broader EL-FWHM of green LEDs than those of blue ones indicates a bigger indium fluctuation through the green active layer.<sup>7</sup> This is in agreement with the AFM measurements we have discussed in section 2.2.2 (Figure 4 and Figure 5).

The radiant power of the various devices was measured as a function of injection current in continuous wave injection (not shown). Device B<sub>LEO</sub> achieved 2.6 times more power than B<sub>Conv.</sub> whereas G<sub>LEO</sub> and G<sub>Conv.</sub> had almost the same peak power independent of the template. In near field EL studies of device B<sub>LEO</sub>, we have observed a stronger luminescence originating from the wing regions compared to the opening regions. This luminescence difference should be related to the density of dislocations on the corresponding regions, demonstrating the role of dislocations as non-radiative recombination centers.<sup>9</sup> For G<sub>Conv.</sub> and G<sub>LEO</sub>, we did not observe any difference between luminescence in the wing and opening regions. This supports our reverse bias analysis, and reinforces that the green LED performance is dominated primarily by the active layer quality. In summary, green MQW quality should be improved to reveal the benefits of GaN LEO templates in green LEDs.

## 2.4 Conclusion

A five-step LEO GaN growth technique for high quality LEO GaN growth is introduced. Blue and green emitting active layers and LEDs on conventional GaN and five-step-grown LEO GaN templates are realized. AFM, XRD and PL are used to study the structural and optical properties of the active layers, and the effects of dislocations on blue and green active layers are identified. Significant differences in blue and green

active layer surfaces are analyzed. The high quality LEO templates are observed to be important for smoother active layer surface morphologies. Blue and green LEDs on conventional GaN and high quality LEO GaN are studied. Green LEDs are observed to be leakier than blue ones, and no significant differences between green LEDs on conventional GaN and LEO GaN in terms of I-V behavior and peak power are observed. Green MQW quality is determined to be the bottleneck for high performance green emitters, not template dislocation density.

### 3 Green Light Emitting Diodes

#### 3.1 Introduction

We have performed room temperature photoluminescence (PL) studies on active layers with peak emission wavelengths of 406 nm, 424 nm, 448 nm, 481 nm, 501 nm, 517 nm, 542 nm, 560 nm, and 570 nm as seen in Figure 12(a). With increasing emission wavelength, a significant decrease in peak emission intensity as shown in Figure 12 (b) is observed. In addition, the longer the emission wavelength the broader the emission spectrum becomes, as seen in Figure 12 (c). The decrease in the intensity is related to dislocations generated due to the high indium content InGaN and GaN. The similar intensity decrease is observed even on our high quality LEO samples.

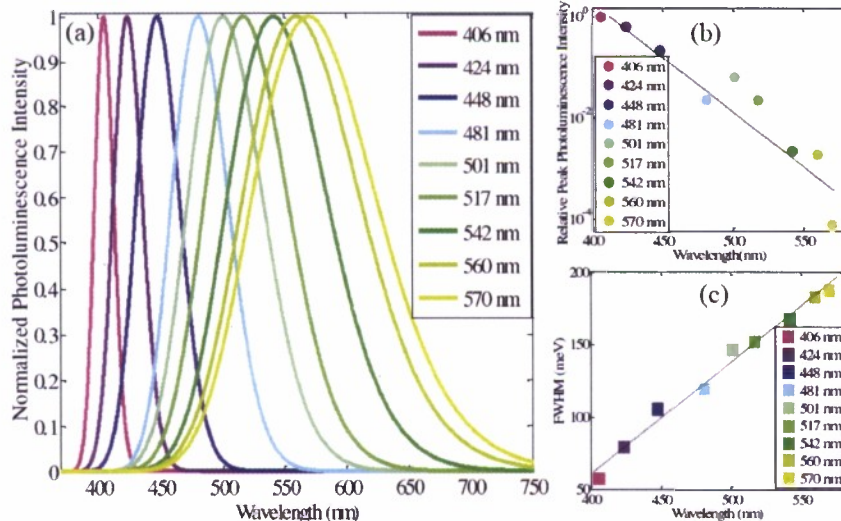


Figure 12. (a) Normalized photoluminescence intensity versus wavelength at 300 K, (b) relative PL peak Intensity (log scale) versus wavelength, (c) FWHM versus wavelength

In order to improve the performance of longer wavelength devices we investigate a novel pulsed growth technique. Using pulsed growth can increase the mobility of the adatoms helping them to diffuse till they settle on the correct lattice site. Mobility could be increased by increasing temperature, decreasing the group III element amount, decreasing the pressure. However, increasing temperature and decreasing pressure results in much lower In content in the layers. We have decreased the total group-III amount as feasible as possible, to a growth rate value of 1.18 nm/min. To give the adatoms more mobility, we developed a pulsed layer epitaxy method, without sacrificing emission wavelength, which improved the active layer significantly.

### 3.2 Experiment

The pulsed atomic layer epitaxy of InGaN is developed to increase the material quality through increasing the mobility of the adatoms. According to our research, a continuous supply of indium is used whereas gallium is pulsed as indium desorbs from the surface quickly and results a decrease in wavelength.

$T_{In}$	$T_{Ga}$	$T_{Total}$	No of Periods	AFM Roughness ( $1\mu\text{m} \times 1\mu\text{m}$ )
4	1	4	39	2.68 Å
4	2	4	39	3.81 Å
4	3	4	39	3.75 Å
4	4	4	39	4.42 Å
2	1	2	78	3.75 Å

Table 3: Effect of pulsing time and period on the surface roughness.

In Table 3, the effect of the pulsing time of gallium and pulsing period time is summarized. The active layers are capped with 7 nm GaN. It is seen that with increasing Ga duration time, the surface roughness increases (Figure 13). In contrast, by decreasing the pulsing period a smoother surface is achieved, as shown in Figure 14.

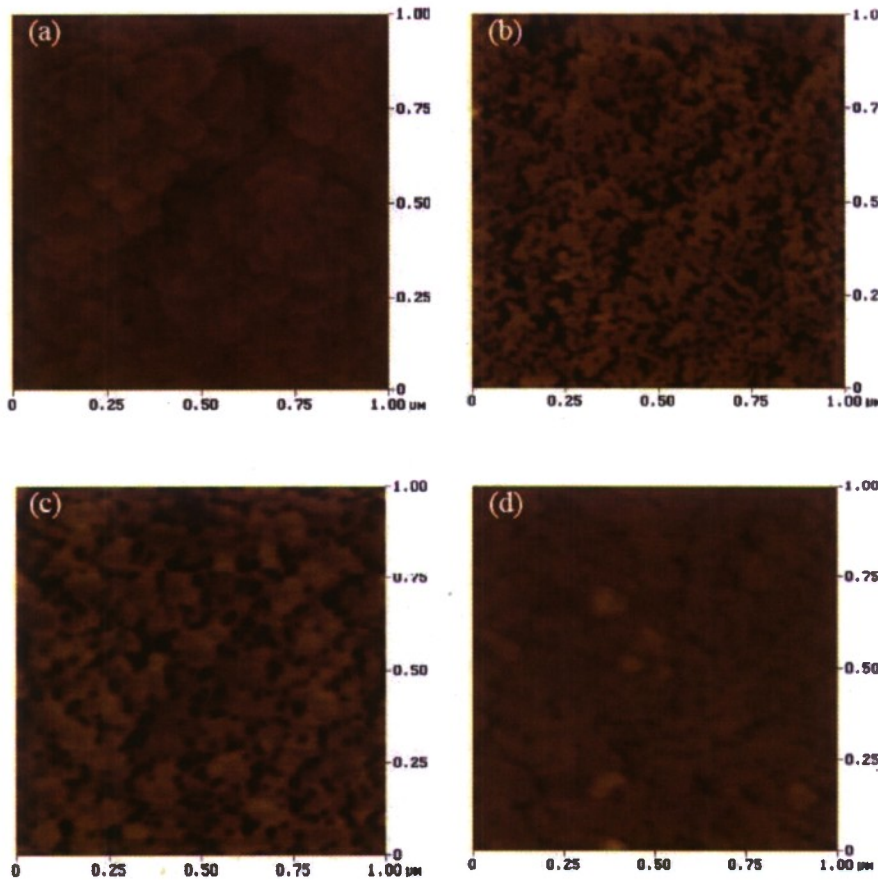


Figure 13. Effect of Ga pulsing time on surface morphology: (a) 1 sec, (b) 2 sec, (c) 3 sec, and (d) 4 sec.

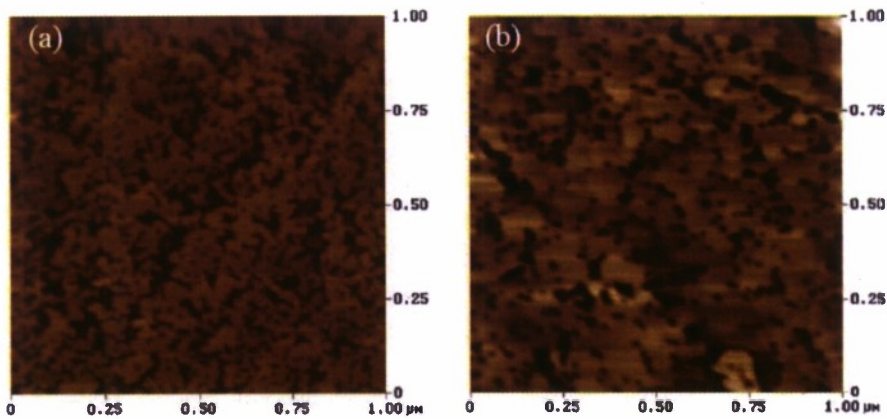


Figure 14. Effect of one period time on surface morphology: (a) 4 sec total, (b) 2 sec total.

During our research, we have observed that the amount of indium in the active layer is strongly effected by the surface on which active layer is grown. At the same growth temperature, on higher quality GaN, InGaN has a lower indium composition. This also suggests that for multiquantum well growths, as the barrier material is grown at low temperatures and layer quality decrease, the indium content of the resulting active layers increase. This results in a broader emission, and if indium is clustered too much, the failure of light emission. We have resolved this problem by employing a temperature cycling in the active layer (Figure 15). To achieve a narrower emission, first a low temperature layer thick enough to keep indium inside at barrier growth temperature is grown. After this low temperature layer, higher temperature GaN is grown.

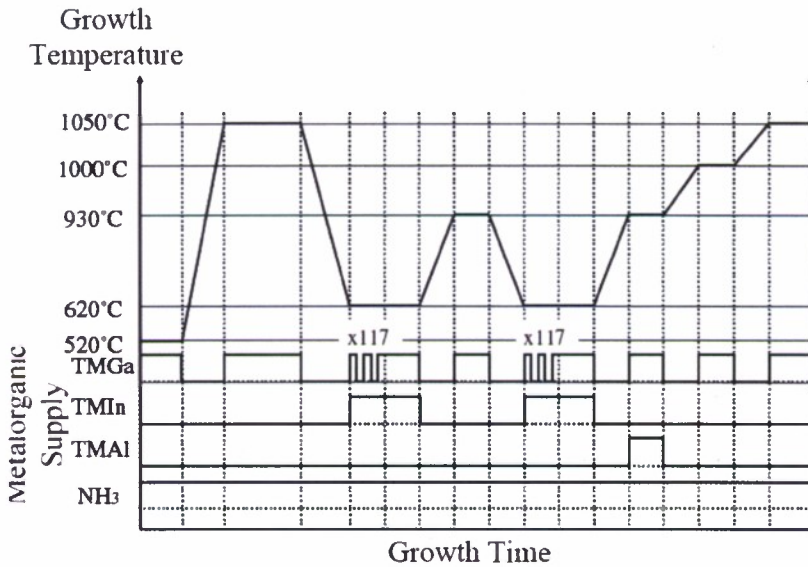


Figure 15. Growth Temperature and Metalorganic Supply throughout the LED growth

Once the LEDs are grown, activation of the *p*-type GaN is achieved by rapid thermal annealing (RTA) at 1000 °C for 30 seconds. After surface treatment with HCl:H<sub>2</sub>O (1:1), 30 Å Ni / 30 Å Au is deposited as transparent contact and is annealed to achieve ohmic contact to *p*-type material. ECR-RIE system (using a SiCl<sub>2</sub> and Ar chemistry) is then used

to etch  $300 \mu\text{m} \times 300 \mu\text{m}$  mesas.  $400 \text{ \AA}$  Ti /  $1200 \text{ \AA}$  Au is finally deposited as the thick contact metal for both *n*- and *p*-type GaN.

### 3.3 Result and Discussion

The devices have a turn on voltage of 6.2 V with turn-on resistance  $\sim 90 \Omega$  (Figure 16). The electroluminescence spectrum is shown in Figure 17.

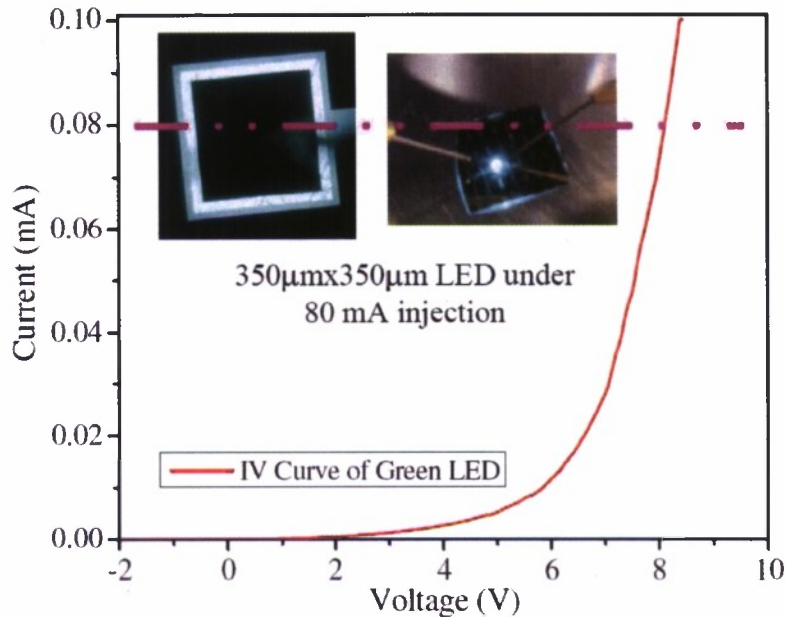


Figure 16. Current Voltage characteristics of a green LED. Inset pictures display a  $300 \mu\text{m} \times 300 \mu\text{m}$  LED under  $80 \text{ mA}$  current injection.

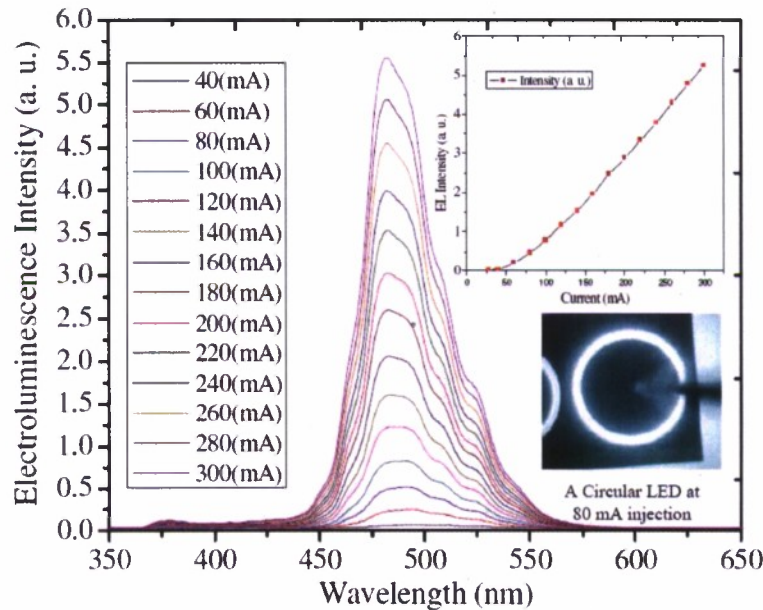


Figure 17. Current Dependent Electroluminescence of the Green LED. Inset displays the current dependence of the peak intensity.

### 3.4 Conclusion

The active layer quality is improved by using pulsed atomic layer epitaxy for InGaN. Thermal cycling in the active layer is developed to ensure uniformity and quality of the quantum wells. We have demonstrated green LEDs with emission wavelength 510 nm at 20 mA. A blue shift with injection current similar to blue LEDs are observed.

## 4 InGaN Quantum Dots for Green Emission

### 4.1 Introduction

The development of high efficiency green LEDs is a crucial part of developing solid state white lighting to replace current inefficient (white) light sources among many other applications like full color displays.<sup>37</sup> With increasing indium content (from violet to green emission), a significant decrease in performance is observed in light emitters based on quantum wells.<sup>38</sup> One of the reasons is that the large lattice mismatch between high indium content InGaN and GaN induces the generation of dislocations in the active region.<sup>38,39</sup> This explains how the performance decreases for high indium content light emitters, even on low dislocated templates.<sup>40</sup> The use of quantum dots may be one way to overcome these limitations in higher indium content devices. Optoelectronic devices based on QDs have many advantages over those based on QWs such as temperature stability and higher efficiency.<sup>41</sup>

Room temperature blue emission from QDs has been reported earlier.<sup>42,43</sup> The strong luminescence from these QDs is attributed to the exitonic transitions.<sup>44</sup> The blue QDs are being integrated into LEDs.<sup>45</sup> However, there are few reports of InGaN quantum dots in the green spectral region at room temperature.<sup>46</sup> In this section, we study the formation of InGaN QDs for green emission, and compare their optical properties with those of InGaN QWs at room temperature. GaN capping of the InGaN QDs for integration into optoelectronic devices is also analyzed.

### 4.2 Experiment

The InGaN layers are grown on 2  $\mu\text{m}$  GaN on double side polished (DSP) (00.1) sapphire ( $\text{Al}_2\text{O}_3$ ) substrate using a horizontal-flow low-pressure metal organic chemical vapor deposition (MOCVD) reactor. The growth rate is 1.18 nm/min and growth is interrupted for 15 seconds under ammonia before cool down. We have studied the effect of temperature, deposition thickness and V/III ratio on the formation and optical quality of the InGaN QDs. After optimization, QDs emitting in deep green, InGaN/GaN QWs emitting in the same wavelength are grown for comparison.

### 4.3 Result and Discussion

Atomic force microscopy (AFM) is used to study the QD formation. Figure 18 (a,b,c) displays the (1  $\mu\text{m} \times 1 \mu\text{m}$ ) AFM images of 4.8 monolayer (ML) InGaN grown at 734 °C, 679 °C, and 633 °C, respectively. As seen in Figure 18 (a,b), at lower temperatures, smaller InGaN disks are observed. These quantum disks will be studied latter. The decrease in disk size is attributed to the decrease in adatom mobility. The decrease in adatom mobility has two main contributors: (1) Decrease in the growth

temperature, (2) Increase in the amount of indium adatom due to higher indium thermodynamic equilibrium at lower temperatures. Effecting both the thermodynamic (indium content in InGaN) and kinetic (mobility) equilibrium on the surface, temperature is the most crucial parameter of interest. We have determined 633 °C to be the ideal temperature in our reactor for the growth of green emitting QDs.

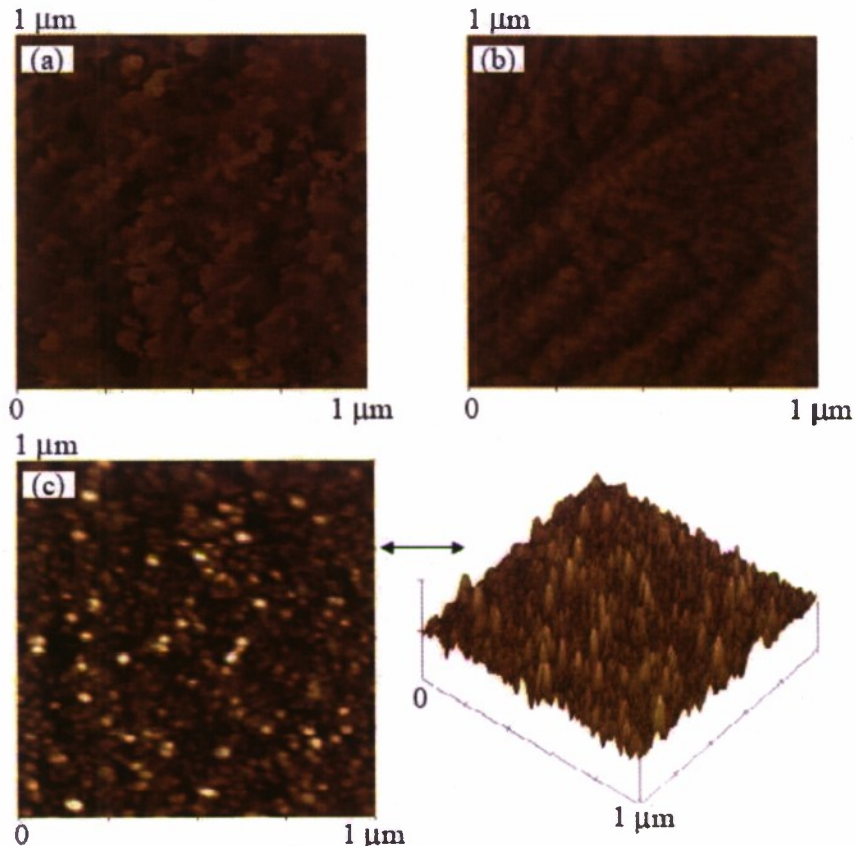


Figure 18. AFM ( $1 \mu\text{m} \times 1 \mu\text{m}$ ) images of 4.8 ML InGaN grown at (a)  $T = 734^\circ\text{C}$ , (b)  $T = 679^\circ\text{C}$ , and (c)  $T = 633^\circ\text{C}$ .

Figure 19(a,b,c) displays the ( $1 \mu\text{m} \times 1 \mu\text{m}$ ) AFM images of 2.4, 3.6, and 4.8 ML-thick InGaN grown at  $633^\circ\text{C}$ , respectively. At  $633^\circ\text{C}$ , we have determined the critical thickness to be  $\sim 3.3$  ML. Below the critical thickness, no QDs are formed (and the surface is similar to Figure 19 (a)). Above this critical thickness, increasing the deposited material results in increase in the density of the QDs at the expense of uniformity (Figure 19 (b,c)). A logarithmic decrease in room temperature (RT) photoluminescence (PL) intensity and linear increase in wavelength with increasing thickness are observed as shown in Figure 20. The intensity decrease is mainly attributed to the increasing number of dislocations in the QDs with their increased size. The wavelength shift may be due to the ground states becoming closer with bigger QDs. More related analysis will be conducted in the future.

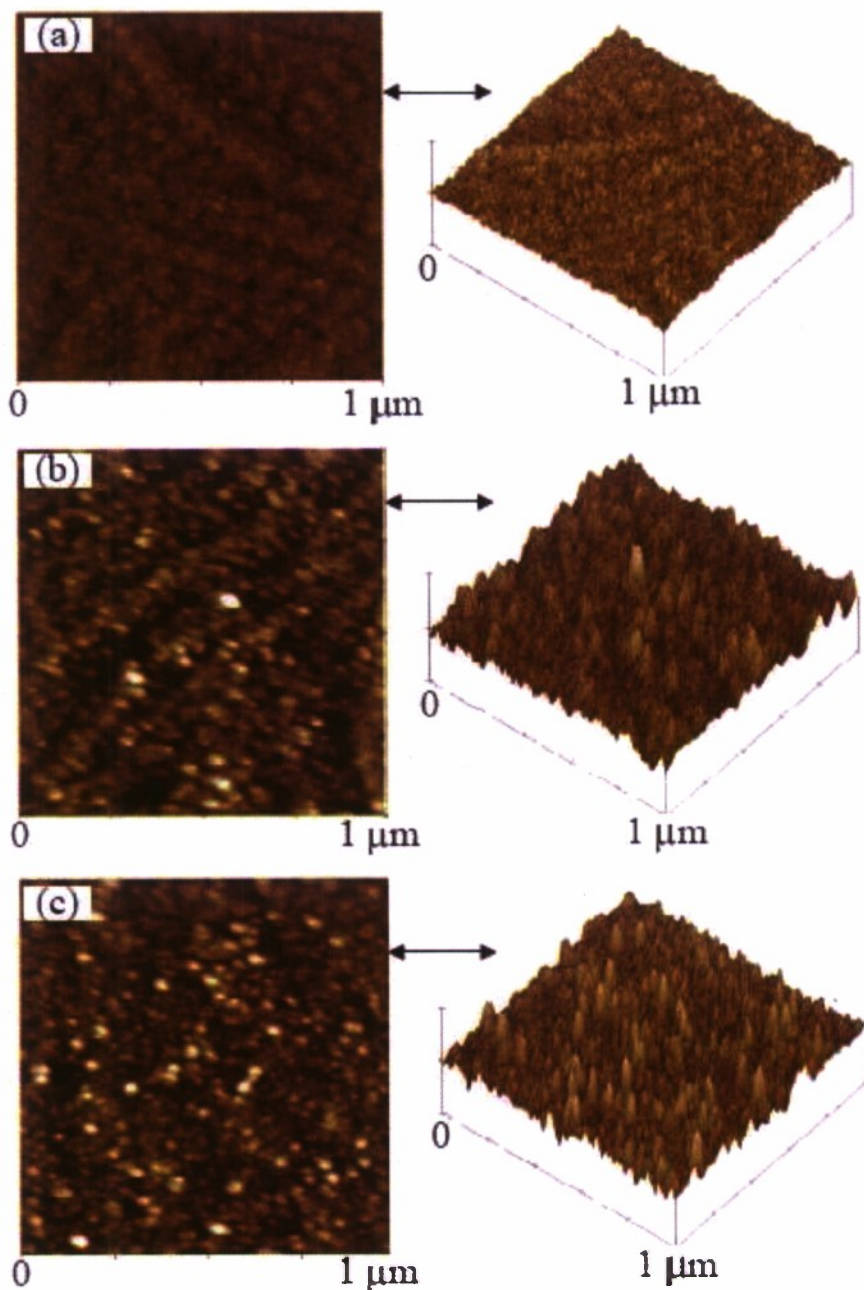
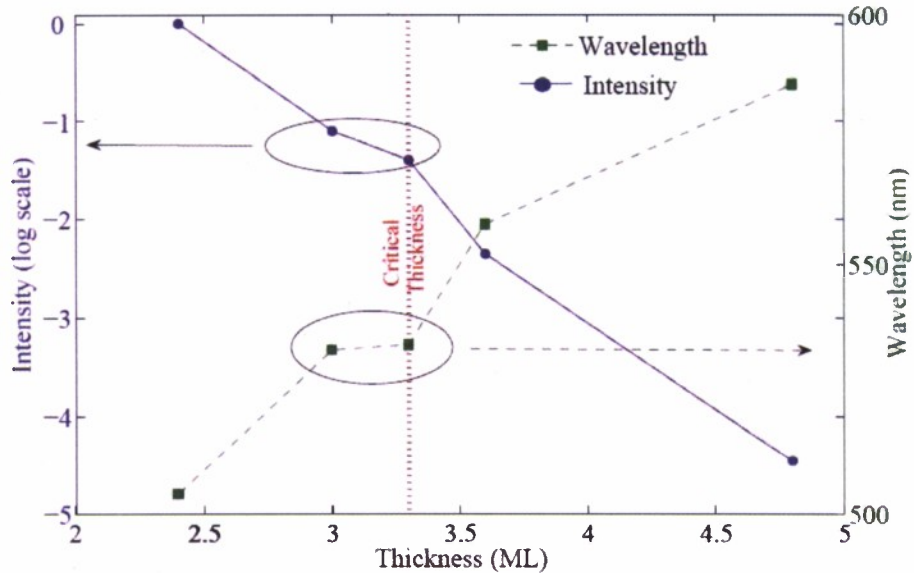
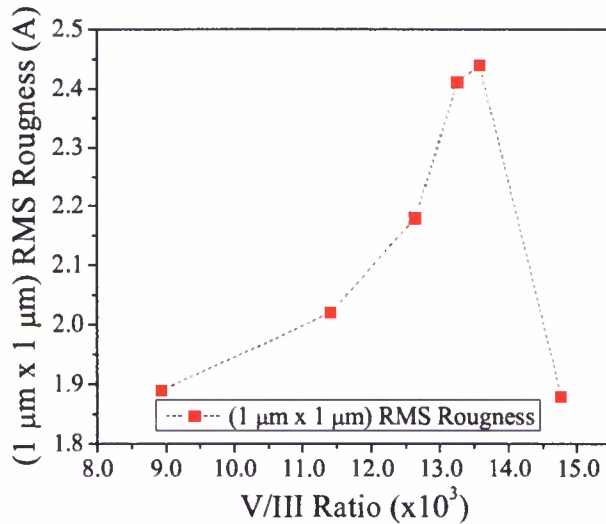


Figure 19. AFM ( $1 \mu\text{m} \times 1 \mu\text{m}$ ) images of (a) 2.4 ML, (b) 3.6 ML, and (c) 4.8 ML InGaN grown at  $T = 633^\circ\text{C}$ .



**Figure 20.** Room temperature photoluminescence intensity and wavelength dependency of InGaN on deposition thickness.

The effect of V/III ratio on the surface morphology is studied. Figure 21 displays the AFM roughness ( $1 \mu\text{m} \times 1 \mu\text{m}$ ) of 3.3 ML InGaN layer vs. V/III ratio at growth temperature  $T = 633^\circ\text{C}$ . For this deposition thickness and temperature, no QDs are observed. As seen in Figure 21, V/III ratio strongly affects the surface roughness. We have determined  $13.88 \times 10^3$ , where the roughness is maximized in Figure 21, to be a good V/III ratio for QD formation at  $633^\circ\text{C}$ .



**Figure 21.** AFM RMS roughness ( $1 \mu\text{m} \times 1 \mu\text{m}$ ) versus V/III ratio for 3.3 ML InGaN grown at  $T = 633^\circ\text{C}$ .

Figure 22 (a,b) displays the ( $1 \mu\text{m} \times 1 \mu\text{m}$ ) AFM images of 4.8 ML-thick InGaN grown at  $633^\circ\text{C}$  with V/III ratio being  $13.88 \times 10^3$  and  $13.57 \times 10^3$ , respectively. As

seen, higher V/III ratio results in bigger quantum dots. V/III ratio being  $13.88 \times 10^3$ , increasing or decreasing V/III ratio results in less uniform quantum dots.

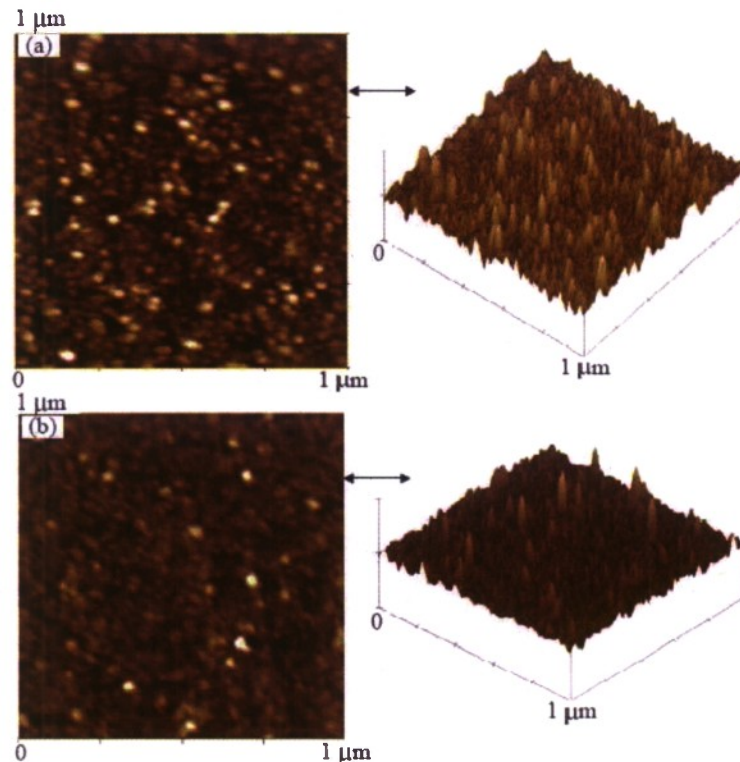


Figure 22. AFM ( $1 \mu\text{m} \times 1 \mu\text{m}$ ) images of 4.8 ML InGaN grown at  $T = 633$  °C with V/III ratio (a)  $13.88 \times 10^3$ , and (b)  $13.57 \times 10^3$ .

Maintaining the growth temperature at 633 °C, and V/III ratio at  $13.88 \times 10^3$ , we have identified two quantum structures: quantum disks and quantum dots both having high optical luminescence at room temperature.

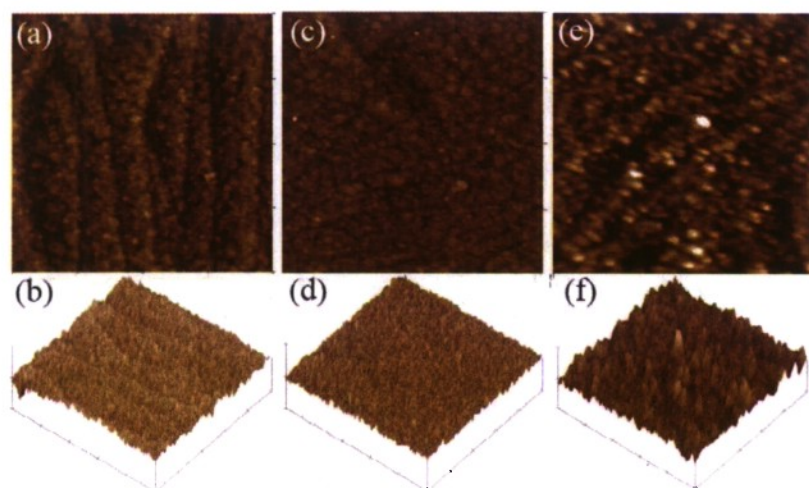
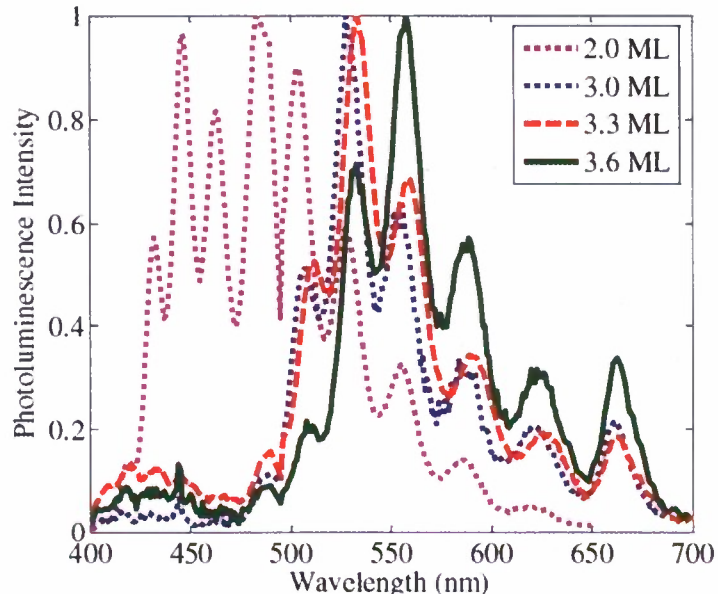


Figure 23. AFM ( $1 \mu\text{m} \times 1 \mu\text{m}$ ) contour and surface images of (a,b) 3 ML, (c,d) 3.3 ML, and (e,f) 3.6 ML InGaN deposition at  $T = 633$  °C.

Figure 23 (a,b) displays the ( $1 \mu\text{m} \times 1 \mu\text{m}$ ) AFM images of 3.0 ML InGaN grown on GaN. The atomic steps are still recognizable and InGaN quantum disks are formed. These quantum disks are the result of elastic InGaN relaxation. At 3.3 ML, the atomic steps become less pronounced (Figure 23(c,d)). When 3.6 ML InGaN is deposited, InGaN QDs are formed (Figure 23 (e,f)). The average size of the quantum dots are 6 Å in height and 40 nm in diameter, and their density is  $5 \times 10^{10} \text{ cm}^{-2}$ .



*Figure 24. Normalized photoluminescence intensity versus wavelength at room temperature for 2, 3, 3.3, and 3.6 ML-thick InGaN.*

We have studied the photoluminescence (PL) of the InGaN QDs at room temperature (Figure 24). The 244 nm line of Argon laser is used for excitation. Fabry-Perot reflections (Figure 24 and Figure 25) are observed due to 2  $\mu\text{m}$  thick cavity formed by the GaN template. At 558 nm, calculated Fabry-Perot peak separation is 34 nm, not far from what we experimentally observe.

With optimized growth conditions, InGaN relaxes into two different quantum structures, quantum disks or quantum dots, dependent on the deposited thickness. For 2 ML of InGaN, the layer is pseudomorphic, and broadband emission from 420 nm to 520 nm is observed. For 3 ML deposition, the layer tends to partially relax by forming 2D quantum disks, shown in Figure 23 (a,b), which leads to two distinct PL bands in Figure 24. The first band (420–460 nm) present a lower emission intensity, and it is attributed to a wetting layer. The existence of this wetting layer is due to Stranski-Krastanow growth mode. The dominant band has a peak at (525 nm), and corresponds to emission from the higher indium content quantum disks. At a thickness of 3.6 ML, quantum dot formation occurs, as shown in Figure 23 (e,f). Two PL bands are also observed, but the high indium content band corresponding to QD emission has a longer wavelength (558 nm) than that of the quantum disk. In conclusion, QD formation takes place after deposition of critical thickness of about 3.3 ML with an apparent PL redshift.

The photoluminescence results from similar InGaN QDs and InGaN QWs are compared in Figure 25. QW and QD structures consist of 3 MQW (3 nm InGaN / 7 nm

GaN) and 3.6 ML InGaN QDs, respectively. However, the PL intensities are comparable, as seen in Figure 25. The QDs have a 117 meV full-width at half-maximum (FWHM) which is narrower than the 165 meV for the QWs at 558 nm. This FWHM is smaller than other published values.<sup>46,47,48</sup> Besides, with increasing excitation, as seen in the inset of Figure 25, FWHM of the QDs decrease whereas that of the QW remains constant. The lower initial FWHM and decrease of FWHM with increasing excitation power is due to QDs having fewer dislocations than QWs. Active layer relaxes elastically by QD formation, and avoids dislocation generation. Comparison of the PL of these QDs and similar QWs shows the higher optical quality of the InGaN QDs, and indicates that a green light emitting device based on InGaN QDs should outperform one based on QWs.

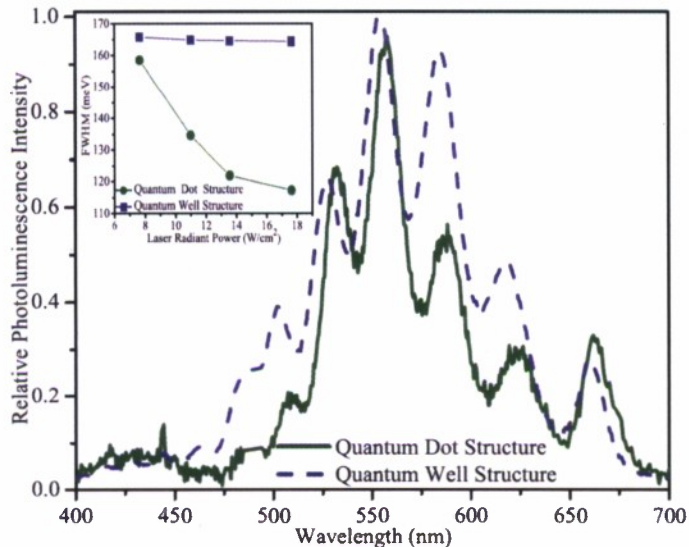


**Figure 25.** Relative photoluminescence intensity versus wavelength at room temperature for QD and QW structures. Inset displays FWHM dependence on incident laser radiant power for QDs and QWs structures.

In ref. [49], the detrimental effect of quantum dot height on radiative lifetime is reported. The strong room temperature luminescence of our QDs should be due to smaller QD height leading to a higher overlap between electron and hole wave functions.

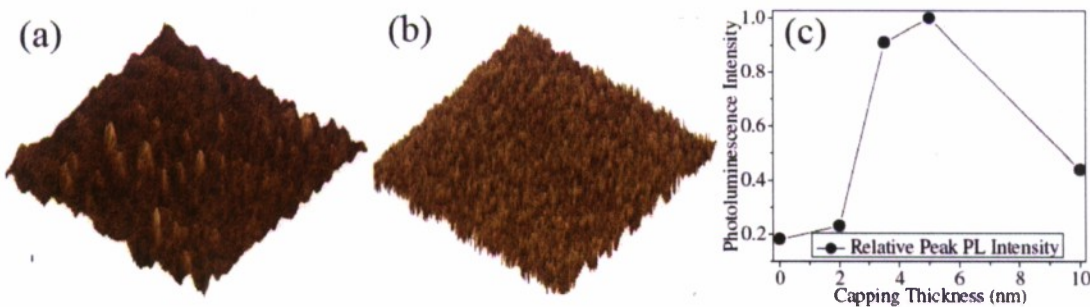


**Figure 26.** AFM Surface Plot for (a) 2 nm capped ( $1 \mu\text{m} \times 1 \mu\text{m}$ ), (b) 5 nm capped ( $5 \mu\text{m} \times 5 \mu\text{m}$ ) 3.6 ML InGaN QDs. (c) Peak photoluminescence intensity dependence on capping thickness.

Incorporating the QDs into LEDs requires an appropriate means of capping the QDs. We have investigated a low temperature GaN capping layer for use with 3.6 ML InGaN QDs. For a 2 nm thick capping layer, we can still resolve the QDs by AFM (Figure 26(a)). However, with 5 nm, the QDs are completely covered (Figure 26(b)). The PL intensity dependence on capping thickness is shown in Figure 26(c). When just covered, the PL intensity increases. However, a thicker capping layer reduces the emission intensity due to the absorption losses in the thick GaN capping layer.

## 5 Novel Inverted Hybrid Green LEDs Based on *n*-type ZnO and InGaN MQWs

### 5.1 Introduction

Although ultra-bright and efficient blue InGaN-based light emitting diodes (LEDs) are readily available<sup>50</sup>, the performance of InGaN-based green LEDs is still relatively poor.<sup>51,52,53</sup> This is because the higher indium content required in the active layers for green emission poses growth problems which lead to performance reduction.<sup>53, 54</sup> As well as phase separation and indium precipitation, one of the main issues is that the elevated substrate temperature (Ts) necessary for the *p*-type GaN top layer causes indium to leak out of the active layers in the InGaN/GaN multi-quantum wells (MQW).<sup>55</sup> This significantly reduces the brightness, efficiency and lifetime of the LEDs.

ZnO is a wide bandgap material (Eg = 3.3 eV) with a large exciton binding energy (60 meV). It has a low toxicity and the same wurtzite structure as GaN. The small in-plane lattice mismatch (~1.8%) with GaN makes ZnO a good candidate for integration in nitride devices.<sup>56,57</sup> Recently, there have been many reports of ultraviolet emitters based on *n*-ZnO/*p*-GaN heterostructures.<sup>58,59,60</sup> In this section, ZnO is adopted as the *n*-layer in a new kind of hybrid green LED.<sup>61</sup>

In conventional GaN-based LEDs, the *p*-layer is deposited on top of the *n*-layer, because the *n*-layer can be grown with higher crystallographic and morphological quality than the *p*-layer. In this work, we adopted an inverted LED structure employing an *n*-ZnO layer grown on top of (In)GaN MQW/*p*-GaN/AlN/Sapphire. Through the use of pulsed laser deposition (PLD), a high quality *n*-ZnO layer could be grown at significantly lower Ts than is typically required for GaN growth in metalorganic chemical vapor deposition (MOCVD). This approach could be beneficial, particularly for green light emitters, in which, the high In content InGaN active layers are adversely affected by the high Ts required for the GaN growth. Furthermore, the refractive index of ZnO at 500 nm is 2.0 compared with 2.5 for GaN. Thus, lower critical angle loss is expected for light extraction through ZnO-capped LEDs.

In this section, we explain the fabrication of these hybrid LEDs, and investigate the optical, structural, and electrical characteristics of the fabricated devices.

### 5.2 Experiment

The AlGaN compounds were grown in an AIXTRON 200/4-HT horizontal flow, low pressure MOCVD reactor. Trimethylaluminum (TMAI), Trimethylgallium (TMGa), Trimethylindium (TMIn), and Bis(cyclopentadienyl)-magnesium (DCpMg) were the metalorganic cation precursors for Al, Ga, In, and Mg sources, respectively. Ammonia

(NH<sub>3</sub>) was used as the nitrogen source. Hydrogen was used as the carrier gas in the AlN and *p*-GaN layers.

First, a 600 nm thick AlN layer was grown on the *c*-sapphire in order to improve the quality of the subsequent *p*-GaN layer.<sup>62</sup> Rapid thermal annealing was realized at 1000°C for 30 seconds in order to activate the Mg dopant. Then, a five period multi-quantum well structure was grown in a nitrogen ambient. Each period consisted of a 2 nm thick InGaN quantum-well with a 4 nm thick GaN barrier. An *n*-ZnO layer was grown on top of the (InGaN/GaN) MQW/*p*-GaN using PLD of a sintered ZnO target with a KrF (248 nm) excimer laser. A ZnO layer was also simultaneously grown directly on *c*-sapphire as a reference for characterization studies.

### 5.3 Results and Discussion

First the structural, electrical and optical properties of hybrid LED layers were reported, and then the effects of solvents, annealing and etching on *n*-ZnO were shown. Thanks to these studies, integration of ZnO in (In)GaN based green LEDs was realized.

#### 5.3.1 Structural characterization of the layers

Scanning Electron Microscopy (SEM) was performed in a Hitachi S4500 microscope equipped with an Oxford Energy Dispersive x-ray microanalysis (EDX) system and Atomic Force Microscopy (AFM) was conducted using a Veeco Dimension 3100 Scanning Probe system.

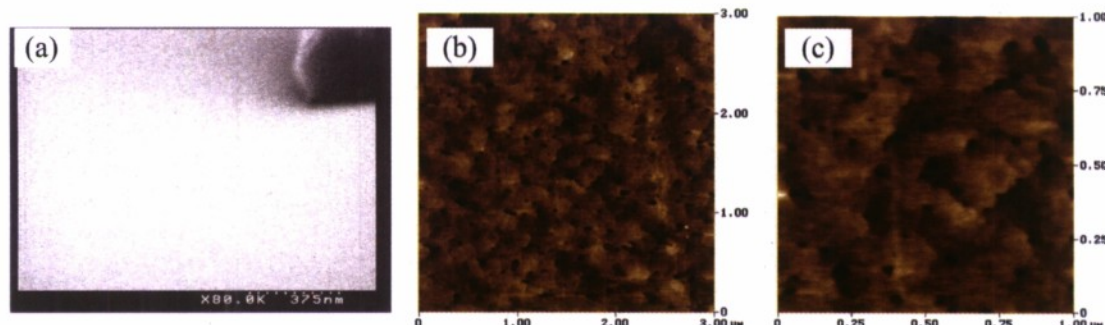


Figure 27. (a) SEM surface micrograph, (b) AFM scan (3  $\mu\text{m} \times 3 \mu\text{m}$ ), (c) AFM scan (1  $\mu\text{m} \times 1 \mu\text{m}$ ) of the surface of *n*-ZnO/Sapphire.

SEM images of the ZnO reference sample surface revealed a relatively featureless morphology (Figure 27(a)), free of the particulates or droplets, which can be an issue with PLD growth. Tapping mode AFM gave root mean square (RMS) roughnesses of 5.6 Å and 4.7 Å for (3  $\mu\text{m} \times 3 \mu\text{m}$ ) and (1  $\mu\text{m} \times 1 \mu\text{m}$ ) scans, which are shown in Figure 27(b) and (c), respectively.

Figure 28(a) shows an SEM micrograph of the top surface of the *n*-ZnO layer of the fabricated hybrid LED. The surface morphology appears rougher than the as-grown *n*-ZnO on sapphire (Figure 27(a)). Figure 28(b) shows an SEM fracture cross-sectional image. The *n*-ZnO / MQW/ *p*-GaN/ AlN/ Sapphire (Al<sub>2</sub>O<sub>3</sub>) LED layers can clearly be distinguished.

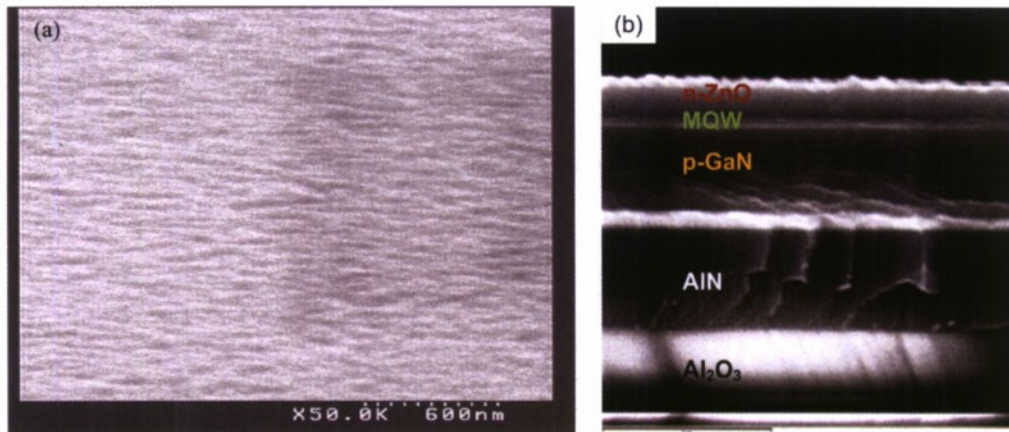


Figure 28. SEM micrographs of the hybrid LED: (a) Surface and (b) Cross-sectional view.

X-ray diffraction (XRD) studies were performed using a High Resolution Panalytical MPD-Pro system Diffractometer.  $\omega$ -2 $\theta$  scans for the (0002) peak of the LED structure are shown in Figure 29. The ZnO and GaN peaks are indistinguishable, suggesting a good lattice match. The MQW-related, satellite peaks are similar before and after the ZnO growth. This indicates that the active layers maintained their compositional and structural integrity.

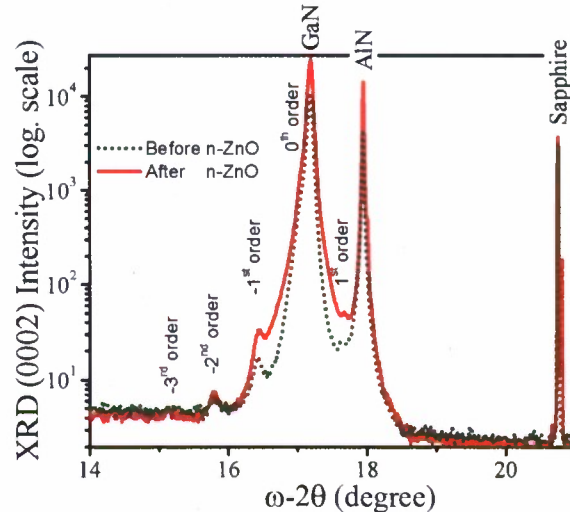


Figure 29. RT XRD  $\omega$ /2 $\theta$  scans for the (0002) peak before and after growth of n-ZnO on the (InGaN/GaN) MQW/p-GaN/AlN/Sapphire.

### 5.3.2 Electrical characterization of the layers

Room temperature Hall effect measurements were performed on the n-ZnO/Sapphire in Van der Pauw configuration (with a magnetic field strength of 0.3 T) with 400 Å Ti/300 Å Pt/1200 Å Au contacts. The n-contacts proved ohmic and carrier concentration was determined to be  $2.8 \times 10^{19} \text{ cm}^{-3}$  with a mobility of  $10.0 \text{ cm}^2/\text{V}\cdot\text{s}$ , and a resistivity of  $0.02 \Omega\cdot\text{cm}$ . Similarly, hole carrier concentration for the p-GaN was determined to be

$7.8 \times 10^{17} \text{ cm}^{-3}$  and 30 Å Ni / 30 Å Au transparent *p*-contacts were observed to be ohmic.

### 5.3.3 Optical characterization of the layers

Photoluminescence (PL) measurements were carried out at RT with a frequency-doubled argon-ion laser at 244 nm. Room temperature PL for the *n*-ZnO/sapphire reference sample revealed a single peak at 377 nm corresponding to the *n*-ZnO band-edge. The spectrum also had relatively low green signal, which implies that there is a relatively low defect density in the sample. Laser power dependent measurements showed no significant peak shift or full-width at half-maximum (FWHM) broadening (Figure 30(a,b)). A linear increase in PL main peak intensity with increasing laser radiant power was observed. These results indicate high optical quality of the ZnO layer.

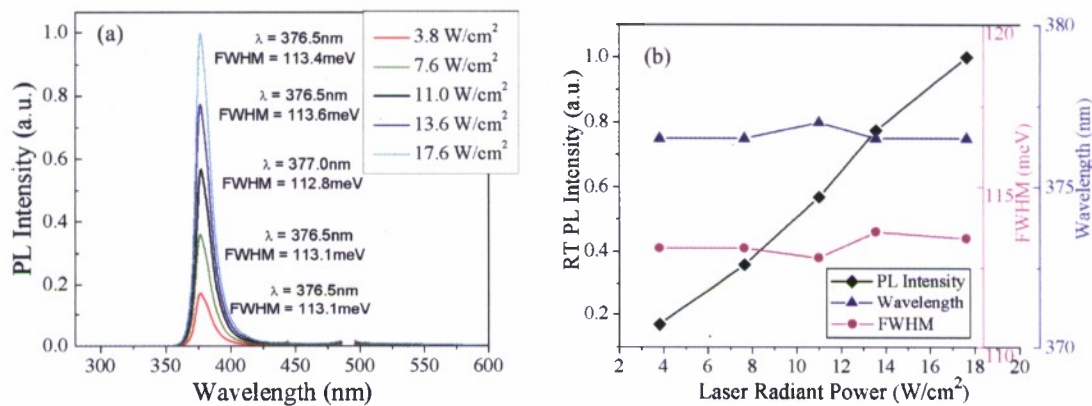


Figure 30. (a) RT PL spectra at different laser powers for *n*-ZnO/sapphire, (b) Peak PL intensity, PL FWHM and wavelength dependency on radiant laser power for *n*-ZnO/sapphire.

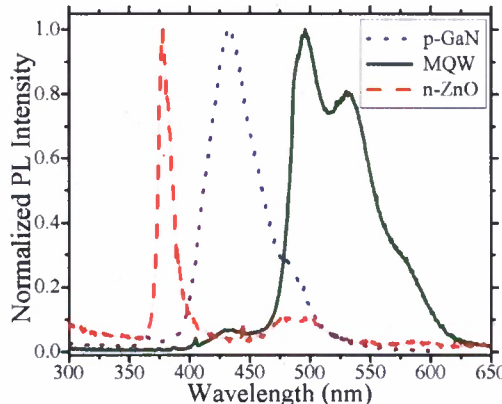


Figure 31. RT normalized PL spectra as consecutive *p*-GaN, InGaN/GaN MQW, and *n*-ZnO layers were grown on AlN/Sapphire.

Normalized RT PL spectra for the hybrid device are shown in Figure 31. The spectrum for the *p*-GaN is dominated by a 426 nm Mg-related peak, which was attributed to defect-related deep level centers.<sup>63</sup> The PL spectrum, once the InGaN/GaN MQWs were grown on the *p*-GaN, shows a strong emission peaked at 496 nm without the

426 nm Mg-related peak. The PL spectrum for the completed hybrid LED structure (including the *n*-ZnO top layer) shows the strongest main emission peak, centered at 376 nm, corresponding to the ZnO band-edge and is similar to the PL observed for the ZnO/sapphire reference sample.

#### 5.3.4 Effect of common solvents on ZnO

The effect on ZnO of the common solvents used in the fabrication of the InGaN LEDs (deionized (DI) water, acetone, trichloroethylene (TCE), methanol and stripper) was studied. After each step, SEM was used to investigate any potential impact on the *n*-ZnO surface. Figure 32 displays SEM micrographs of the initial ZnO surface (a) and the surface after consecutive immersion in (b) ~ 5 min DI water, (c) ~ 5 min acetone, (d) ~ 5 min TCE, (e) ~ 5 min methanol, and (f) ~ 5 min stripper. All solvents were held close to their boiling temperature. No agitation was used. No significant degradation of the *n*-ZnO surface was observed after treatment with these solvents under these conditions.

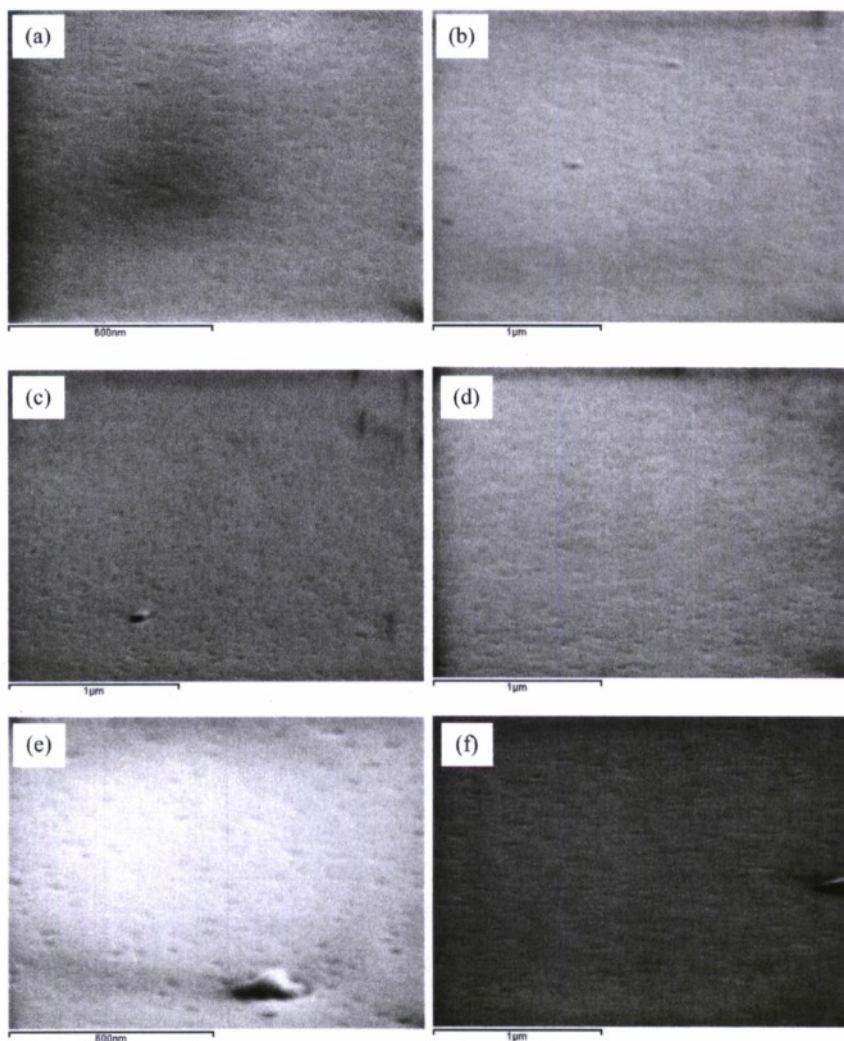


Figure 32. SEM micrographs of (a) the initial *n*-ZnO surface and after treated with (b) DI water, (c) acetone, (d) TCE, (e) methanol, and (f) stripper, consecutively.

### 5.3.5 Effect of annealing

Annealing is a crucial parameter in order to obtain low resistance ohmic contacts to *p*-GaN. Our studies established that 30 Å Ni / 30 Å Au contact to *p*-GaN was least resistive when annealed at 500 °C for 10 mins in air. Thus, an annealing test of the *n*-ZnO layer was realized under this condition. This annealing was determined to damage the *n*-ZnO surface. Thus, *p*-contacts were not annealed for these hybrid LEDs. Evaporated 30 Å Ni / 30 Å Au / 400 Å Ti / 1200 Å Au were found to be ohmic, however. Further studies are being carried on for optimization of annealing with regard to overall LED performance.

### 5.3.6 Etching Study

Dry etching was preferred to wet-etching for consistency and for the realization of better side-wall profiles. A systematic study of dry etching (with a Plasmatherm electron cyclotron resonance reactive ion etching (ECR-RIE) system) was conducted. For the GaN, a (SiCl<sub>4</sub> + Ar) chemistry was adopted based on our prior studies.<sup>64</sup> For the *n*-ZnO, (CH<sub>4</sub> + Ar) chemistry was employed, with Ar at 5 mTorr. A common side-wall angle of ~70° was observed (Figure 33). The *n*-ZnO etch rate was determined to be 53 nm/min.

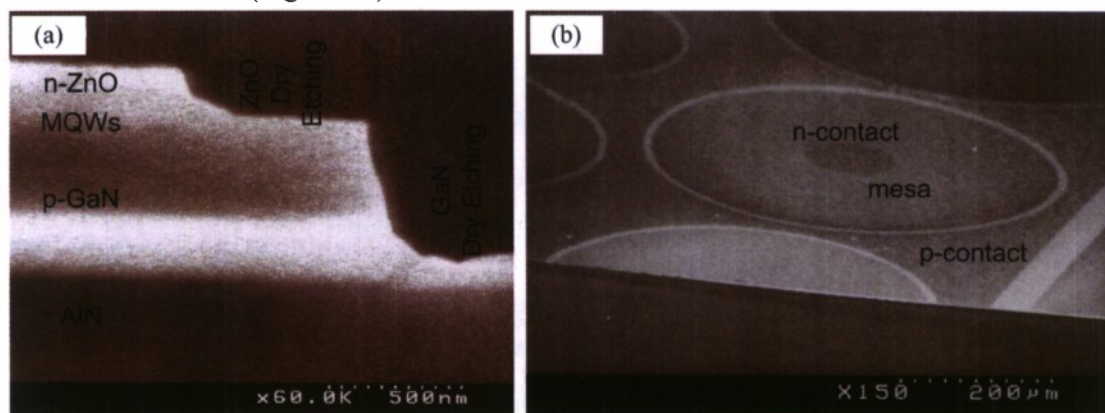


Figure 33. SEM micrographs of a fabricated hybrid LED (a) Side view, (b) Top (angled) view.

The mesa formation of the LED was realized in two steps. First step was the etching of the *n*-ZnO via CH<sub>4</sub>-based chemistry. Then the sample was taken out so that the ECR-RIE system could be seasoned and tested, and the second etching step was realized: etching of the (In)GaN layers via SiCl<sub>4</sub>-based chemistry. One concern in the use of CH<sub>4</sub>-based chemistry is that a C:H (amorphous hydrogenated carbon) or CH<sub>x</sub> polymer-like layer could be easily formed and deposited that may impede the continuous etching reaction.<sup>65</sup> This should be responsible for the two step mesa formation (seen in Figure 33(a)). Solving this issue requires improving the dry-etching profile via optimizing the etching conditions<sup>65</sup> and improving the photoresist selectivity<sup>66</sup> as well as employing inductively coupled plasma. This requires further etching studies for ZnO/(In)GaN heterostructures. Besides, current crowding is known to be an issue in nitride LEDs. The light is mostly emitted from the edges (where *p*- and *n*-contacts are the closest) due to significant mobility difference between electron and holes. Thus, in order to maximize LED performance, single vertical mesa formation should be realized.

In the  $\text{CH}_4$  based plasma, the main etching mechanism of zinc in  $\text{ZnO}$  is the formation of a zinc compound such as  $\text{Zn}(\text{CH}_3)_x$ . The etch product for oxygen is most likely  $\text{O}_2$ , although OH radical may play a role.<sup>66</sup>  $\text{CH}_4$  percentage<sup>65</sup> as well as carrier gas<sup>67</sup> is known to affect the atomic composition of etched  $\text{ZnO}$  surface. In our research, we have used x-ray microanalysis to gather information about the elemental composition of the specimen in terms of qualitative distribution. An etch-test EDX study shown in Figure 34 indicated that etched layers of  $n\text{-ZnO}$  had a lower Zn atom density than the as-grown layer. Al and O atom densities were also observed to be higher on the etched surface relative to those on the as-grown mesa area. Figure 34 (b,c) gives the normalized scale for the EDX count rates for Zn, Al and O atoms for the etched and as-grown layers showing the spatial distribution of elements. Our observation agrees with the strong etching of the zinc (via  $\text{CH}$  radicals<sup>65,66,67</sup>) in  $\text{CH}_4$  based chemistries leading to less zinc concentration in the etched-surface. The relative increase in aluminum and oxygen atoms on etched layer relative to as-grown layer may be related to strong etching of elemental zinc that also leads to a relatively higher XRD counts for oxygen, and aluminum than zinc. This elemental variance is significant as it may effect the carrier concentration as well as optical and structural characteristics of the etched-surface.<sup>68</sup>

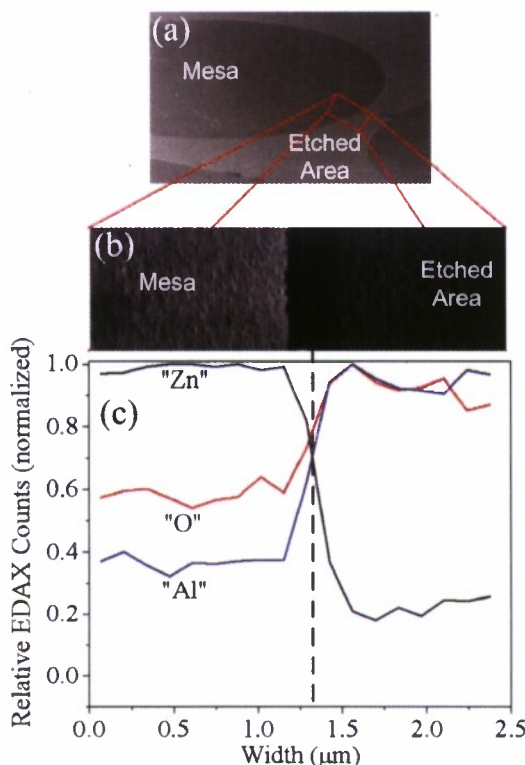


Figure 34. (a) Dry etching of  $n\text{-ZnO}$  on sapphire, (b,c) EDX system analysis shows the relative concentrations of O, Al and Zn atoms through 2.46  $\mu\text{m}$  (from mesa through etched area). The EDX scale is normalized and relative.

### 5.3.7 Device Performance

After optimization of the fabrication process, hybrid green LEDs were fabricated using optimized processing techniques. First of all, the samples were cleaned chemically.

The cleaning steps included TCE, acetone, methanol treatment and rinsing. Circular LED mesas, with an area of  $0.30\text{ mm}^2$ , were fabricated by masking the surface and dry etching right through the *n*-ZnO layer to a depth of 500 nm into the *p*-GaN.

A typical I-V curve for the hybrid LED was given in ref. [69]. The turn-on voltage was around 2.5 V, which was close to the bandgap energy (2.5 eV – 496 nm) observed in the PL spectrum. Reverse bias analysis suggested that hopping conduction was responsible for the leakage current.<sup>69</sup>

Output power of the hybrid LED was measured utilizing a calibrated integrated sphere. Under forward bias, green light was easily observed with the naked eye at RT under continuous-wave (CW) operation. Optical output power was on the order of  $\mu\text{W}$ . Electroluminescence spectra were acquired under pulsed operation (duty cycle of 10%, frequency = 5 kHz) in order to reduce heating effects under higher current injection. EL spectra (Figure 35) revealed an emission peaked in the green regime with a blueshift from 510 nm to 504 nm as the current increased from 400  $\mu\text{A}$  to 1000  $\mu\text{A}$ . The FWHM decreased simultaneously from 194 meV to 179 meV. These effects were attributed to free-carrier screening of the piezoelectric field, which led to bandgap renormalization.<sup>70</sup> The spectral narrowing for the device demonstrated no band-filling effects, even for higher current injections, and thus indicated superior quality of the active layer.<sup>71</sup> This was consistent with the high compositional and structural integrity of the MQWs inferred from the XRD studies (Figure 29) and can be attributed to the lower  $T_s$  employed for PLD of the ZnO top *n*-layer. More device details can be found in ref. [69].

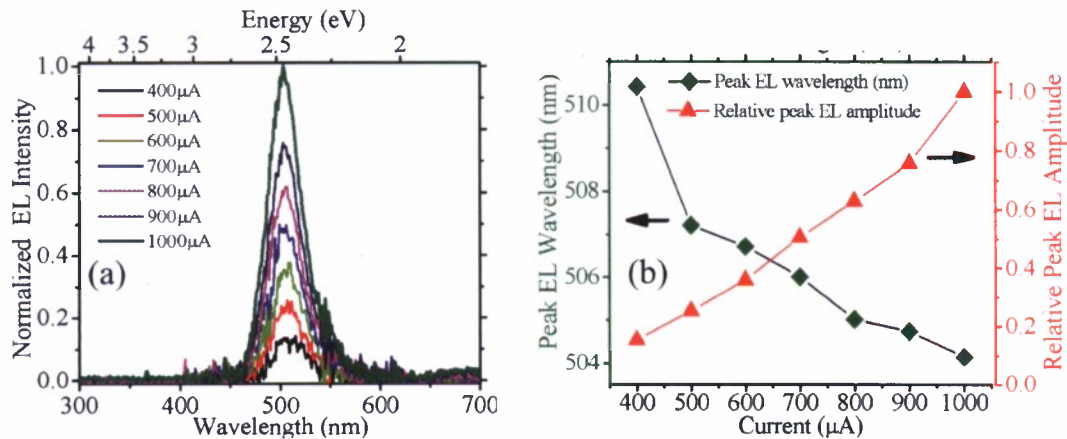


Figure 35. (a) Normalized electroluminescence (EL) intensity of the hybrid green LED at room temperature, (b) Peak EL wavelength and amplitude with respect to injection current.

Further optimization of the hybrid LED design and fabrication process are in progress, including improvement of electron and hole current spreading through adjustment of the *n*-ZnO and *p*-GaN layer thicknesses. *p*-GaN etch-depth is also under investigation, in order to inject holes more uniformly. Thicker green active layers are also being developed, which should give higher output in the green (since the ZnO growth temperature is lower than that for the InGaN, thicker InGaN layers should be more stable).

## 5.4 Summary

Novel hybrid green LEDs were developed. These devices employed an inverted *p-n* structure and the substitution of *n*-ZnO for the *n*-GaN layer. Conventional MOCVD growth was used for the *p*-GaN and MQWs. Lower temperature PLD was adopted for the ZnO growth in order to combat thermal degradation of the InGaN layers. High structural and optical quality of the ZnO, GaN and (In)GaN layers were confirmed using XRD and PL analyses, which suggested that the integrity of the MQW was maintained.

The effects of common solvents, etchants and annealing on *n*-ZnO were investigated. No significant degradation of the *n*-ZnO surface was observed after consecutive treatment with DI water, acetone, TCE, methanol, and stripper. Dry etching of *n*-ZnO with (CH<sub>4</sub> + Ar) chemistry was found to give good side-wall profiles for the device fabrication. Some minor degradation of the *n*-ZnO surface was observed after the 10 minute anneal at 500 °C in air, which is commonly adopted for *p*-GaN transparent contact optimization. Evaporated 30 Å Ni / 30 Å Au / 400 Å Ti / 1200 Å Au and 400 Å Ti / 300 Å Pt / 1200 Å Au contacts were found to give ohmic contacts to the *p*-GaN and *n*-ZnO, respectively, without annealing.

Under these processing conditions, a hybrid LED giving green EL between 510 and 504 nm, with a CW output on the order of μW, at RT was realized. Such an inverted hybrid structure approach could hold the prospect for the development of future green LEDs with superior performance.

## 6 High Optical Response in Forward Biased InGaN–GaN Multiquantum-Well Diodes Under Barrier Illumination

### 6.1 Introduction

From the first investigations in III-nitride semiconductors, the high responsivities observed in GaN photoconductors and the associated gain mechanisms attracted the attention of many groups.<sup>72,73,74</sup> Other structures and photocurrent gain mechanisms have been also studied in order to satisfy the need of high sensitivity ultraviolet (UV) detectors for visible- and solar-blind applications. Examples of this research are: carrier multiplication in avalanche photodiodes,<sup>75,76</sup> minority carrier trapping in Schottky barrier photodiodes,<sup>77</sup> and more recently, piezoelectric field engineering in multiple-quantum-well (MQW) detectors.<sup>78</sup> However, only avalanche multiplication has demonstrated high enough gain (> 10<sup>6</sup>) to show single photon detection capabilities.<sup>79,80</sup>

A wide variety of (Al,Ga)N detector structures have been extensively studied for visible- and solar-blind applications. For detection in the visible and ultraviolet-A, (In,Ga)N/GaN MQW structures have demonstrated reliable performances and internal gain mechanisms as active regions of *p-n* and Schottky barrier photodiodes.<sup>78,81,82</sup> The polarization fields in InGaN/GaN multiple-quantum-well structures introduce additional variables in the carrier recombination dynamics. Charge separation and long recombination times are more likely in the sawtooth potentials created by the piezoelectric effect. High electric fields in the wells and barriers also modify the absorption spectra through the quantum confined Stark and Franz-Keldysh effects, respectively. Although material defects such as Indium non-uniformities across the well

and threading dislocations complicate the analysis, clear features of the presence of strong electric fields have been observed in multiple studies.<sup>83,84,85</sup>

In this work, we investigate an unexpected photocurrent component observed in *p*-(In,Ga)N/GaN multiquantum well (MQW) diodes under forward biases just before the turn-on voltage. Spectral characteristics, linearity, and time response are shown and discussed. These results are interpreted taking into account the absorption in high electric fields, potential distribution and carrier transport. Its application for single photon detection is also discussed.

## 6.2 Sample growth and device fabrication

*p*-InGaN/GaN MQW-N structures were grown on a lateral epitaxial overgrowth (LEO) GaN template by metal organic chemical vapor phase deposition. Details of the LEO technique can be found elsewhere.<sup>86</sup> The *n*-layer consisted of a 1  $\mu\text{m}$  thick GaN:Si layer. The undoped active layer comprised three InGaN/GaN (3 nm/7 nm) quantum wells, and was capped with a 550 nm thick GaN:Mg layer. The indium content in the wells was about 17%. Activation of the *p*-type GaN was achieved by rapid thermal annealing (RTA) at 1000 °C for 30 s. From Hall effect measurements in reference samples, electron and hole concentrations were determined to be  $3 \times 10^{18} \text{ cm}^{-3}$  and  $4 \times 10^{17} \text{ cm}^{-3}$  in the *n*- and *p*-type layers, respectively.

After surface treatment with HCl:H<sub>2</sub>O (1:1), Ni/Au 30 Å/30 Å is deposited as semitransparent contact and is annealed to achieve ohmic contact to *p*-type material. Mesas were defined by ECR-RIE with SiCl<sub>2</sub> and Ar plasmas. Ti/Au (400 Å/1200 Å) is deposited as the thick contact metal for both *n*- and *p*-type GaN. Device sizes ranged from 0.005 mm<sup>2</sup> to 0.07 mm<sup>2</sup>.

Two reference *p-i-n* samples were also grown for the study. The first had an intrinsic region thickness equal to the total length of the active region (30 nm) in the *p*-MQW-*n* structure, and was used to compare electro-optical properties. The second had an intrinsic region of 200 nm and was used to perform electro-absorption measurements in order to determine the effect of the electric field on the GaN absorption cut-off.

## 6.3 Results and Discussion

### 6.3.1 Electro-optical characteristics

Current-voltage (I-V) characteristics were measured in *p*-InGaN/GaN MQW-*n* diodes using an HP4155A Semiconductor Parameter Analyzer under back-illumination. A Xe lamp and a monochromator were used with a UV fiber-optic cable to couple the light, and allow back-illumination of the device. The input slit of the monochromator was adjusted to vary the photon flux, which was calibrated using a NIST traceable UV-enhanced Si detector.

As shown in Figure 36, devices presented two ranges of operation for light detection; one at reverse and low forward voltages, and other between 2.5 and 4.5 V forward bias. The photocurrent signal obtained in the first operation range is the result of the absorption in the active region, and covers the wavelength range from 363 nm to 440 nm. The maximum wavelength corresponds to the onset of absorption in the quantum wells as verified from our optical transmission measurements. The slight increase observed with

the reverse bias is attributed to a reduction of the carrier escape time from the well, which improves the external quantum efficiency, as discussed in ref. [87].

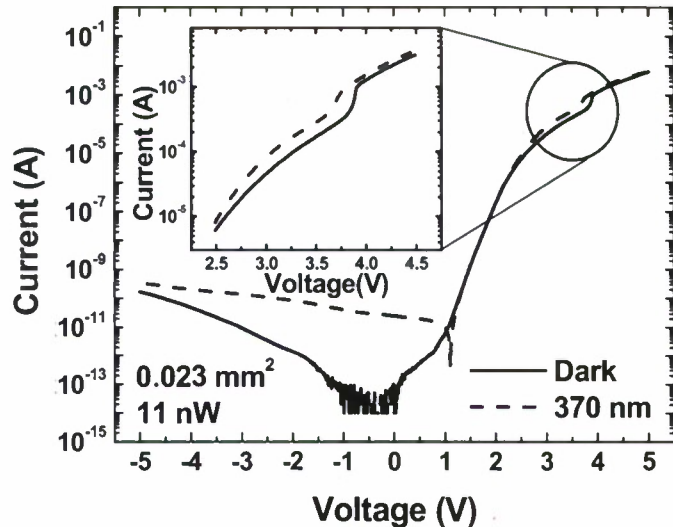


*Figure 36. Current-voltage characteristic measured in darkness (solid line) and under back-illumination (dashed line) with an optical power of 11 nW at 370 nm for a device area of 0.023 mm<sup>2</sup>. Inset: Abnormal photocurrent signal under forward bias.*

The inset of Figure 36 magnifies the second operation range in which an unexpected photocurrent signal is observed just before the turn-on voltage, as well as an unidentified step-like feature, near 4 volts. In contrast to the first operation range, this electro-optical signal was only measured when the device was illuminated with wavelengths between 363 and 375 nm. These characteristics were observed in almost all of the diodes characterized, but they were most evident in the smallest area devices, i.e. those devices with less leakage current. Although the samples under study were grown on an LEO substrate to minimize leakage, we can rule out any effect of the LEO pattern, since the same behavior had been observed in devices on non-LEO substrates. In fact, a similar step-like feature has been observed before in InGaN/GaN Schottky photodiodes under high power excitation at similar voltages, as reported in ref. [88].

From these measurements, an effective gain value was calculated by using  $G(V) = (I_{370\text{nm}}(V) - I_{\text{dark}}(V)) / I_{370\text{nm}}(0)$ , where  $I_{370\text{nm}}$  and  $I_{\text{dark}}$  represent the current under 370 nm and no illumination, respectively, and  $V$  is the operation voltage. Figure 37 shows the gain characteristic for two different size devices. Peak gain values in the  $10^7$  range were obtained; a high value obtainable in the past only by avalanche photodiodes. The gain was slightly higher for smaller area devices. The inset of Figure 37 shows the photocurrent signal relative to the dark current, which reveals two prominent humps under back- or front-illumination with maximums at about 3 V (R1) and 3.8 V (R2), the latter corresponding to the onset voltage of the step-like feature. The origin of these two humps will be discussed later.

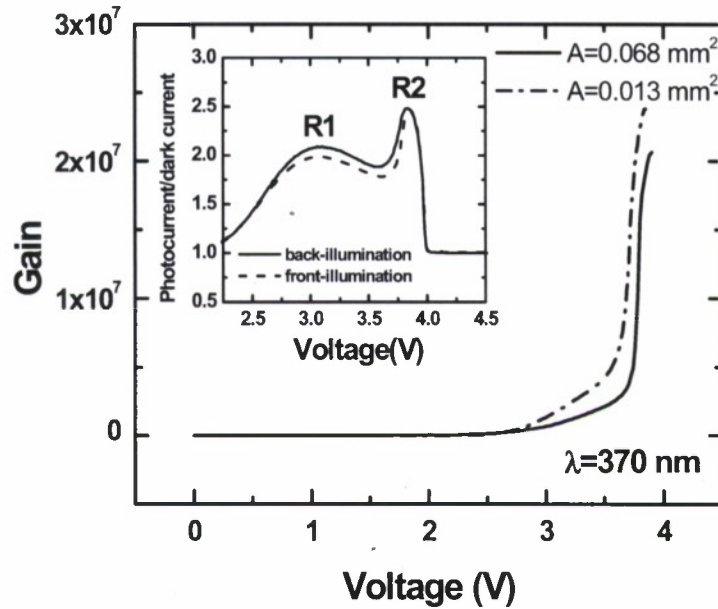


Figure 37. Effective photocurrent gain obtained under illumination at 370 nm in devices with  $0.068$  (solid line) and  $0.013\text{ mm}^2$  (dashed line) areas. Inset: Photocurrent to dark current ratio under back- (solid line) and front-illumination (dashed line). The two bands obtained were labeled as R1 and R2.

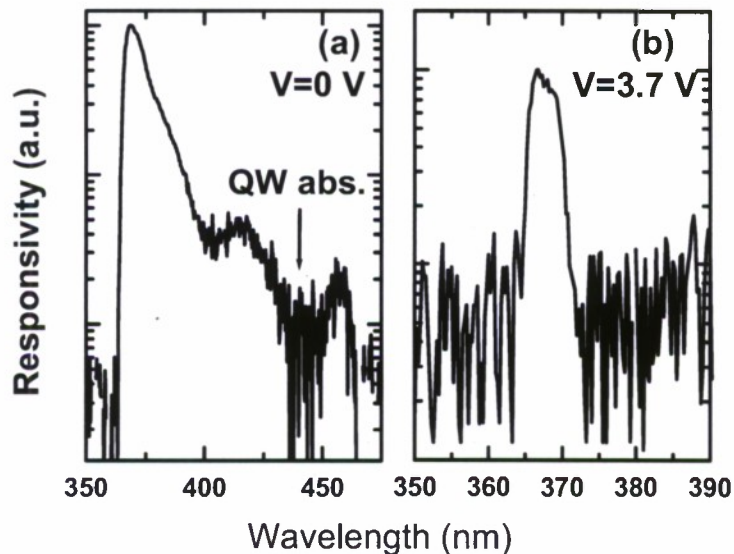
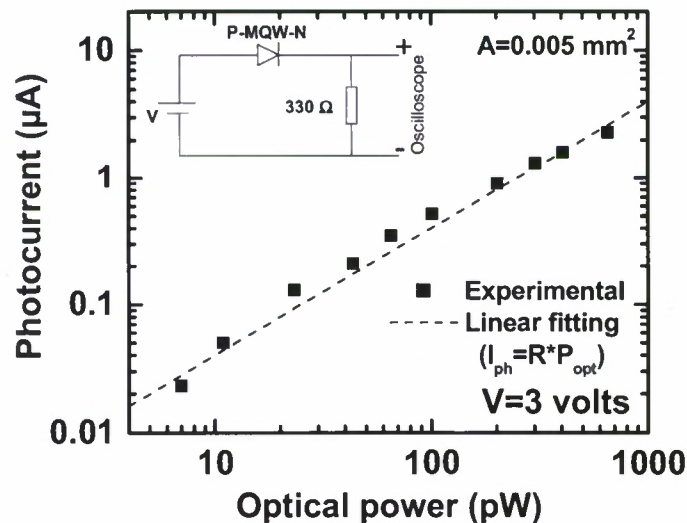


Figure 38. Spectral response of the p-MQW-n diodes measured at (a)  $0\text{ V}$  and at (b)  $3.7\text{ V}$ . The onset of the quantum well absorption is indicated.

The spectral response of the devices under back-illumination was measured at zero bias, in the absence of any gain mechanism, and at  $3.7\text{ V}$  (Figure 38). Under this illumination scheme, the GaN substrate helps to filter out the light with  $\lambda < 363\text{ nm}$  with

a very high rejection ratio,<sup>89</sup> making these detectors well suited to use in fluorescence applications with excitation wavelength lower than 363 nm. At zero bias, the long wavelength response onset situates around 440 nm, in good agreement with the absorption onset in the quantum wells. However, under forward biases, the spectral characteristic of the response differs significantly. The device is only sensitive to a very narrow band from 364 nm (GaN bandgap) to 372 nm.

In order to study the linearity of this response, a  $0.005 \text{ mm}^2$  device was biased at 3 V, i.e. the voltage that maximized the R1 band, in series with a  $330 \Omega$  load resistor (inset, Figure 39). The current was measured via the voltage drop in the resistor using an oscilloscope. The device was illuminated with optical powers lower than 1 nW. As observed in Figure 39, photocurrent scales linearly with optical power, with a peak responsivity of about  $4000 \text{ A/W}$ . The minimum illumination detected was 8 pW without any further amplification or lock-in technique. The minimum detectable illumination increased slightly with device area; thus, 15 pW were needed to produce a significant change over the dark current level in  $0.023 \text{ mm}^2$  devices.



**Figure 39.** Power-dependent measurements obtained from a  $0.005 \text{ mm}^2$  area diode at 3 V. The dashed line is the linear fitting using  $I_{ph}=R \cdot P_{opt}$ , for which  $I_{ph}$  is the photocurrent defined as the total current minus the dark current,  $P_{opt}$  is the optical power, and  $R$  is the responsivity that acts as fitting parameter. Inset: Experimental set-up.

The temporal response of the device at 3 V (R1) and at 3.8 V (R2) was measured (Figure 40). The response at 3.8 V presented a faster rise time than at 3 V. However, after illumination, whereas the sample biased at 3 V recovers its baseline dark current within tens of seconds, at 3.8 V, the current decreases following a non-exponential characteristic, eventually plateauing at an elevated current. The current difference between these two levels corresponds to the amplitude of the step-like feature observed in the I-V characteristic. This can be attributed to an optically induced transition between two states of the device.

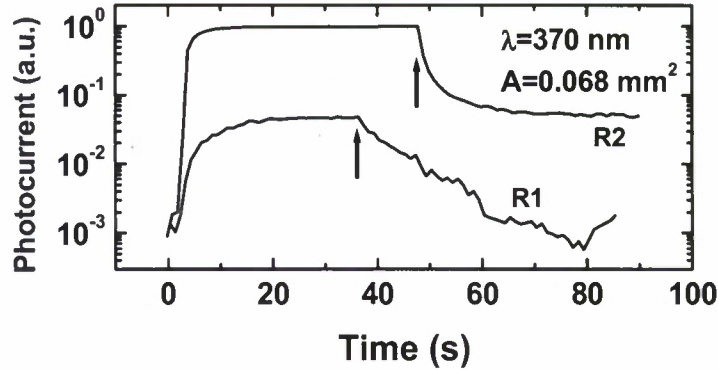


Figure 40. Time response of a  $0.068 \text{ mm}^2$  diode obtained during illumination at  $370 \text{ nm}$  at  $3 \text{ V}$  (R1) and  $3.8 \text{ V}$  (R2). The dark current level at  $t=0 \text{ s}$  was subtracted for clarity. The light is turned on during the first two seconds. The arrows indicate the turn-off.

### 6.3.2 Band diagram

In order to find out the origin of the spectral response characteristic under forward bias, we investigated the band structure. The resolution of the Poisson equation allows us to determine the potential distribution ( $V(x)$ ) in the active region.<sup>90</sup> As a first approximation, we assumed that all the quantum wells are inside the depletion region, and that any unintentional doping there is much lower than the intentional doping of the  $p$ - and  $n$ -type layers. The piezoelectric field in the growth direction ( $F_z$ ) was calculated from  $F_z = P_z / \epsilon_s$ , where  $P_z$  is the polarization as defined in ref. [91], and  $\epsilon_s$  is the dielectric permittivity of GaN. From the linear interpolation between GaN and InN, a 12% difference between the permittivities of GaN and  $\text{In}_{0.17}\text{Ga}_{0.83}\text{N}$  is estimated. This difference is neglected in the analysis. Under these conditions, the analytical solution of the Poisson equation can be expressed as

$$\begin{aligned}
 V(x) = & \\
 \begin{cases} 0, & x < -x_p \\ qN_a(x + x_p)^2 / 2\epsilon_s, & -x_p < x < 0 \\ \frac{qN_a}{\epsilon_s} x_p x + \frac{qN_a}{2\epsilon_s} x_p^2 \\ + F_z \left( \frac{L_b}{L_w + L_b} x - l_w(x) \right), & 0 < x < W \\ -\frac{qN_d}{2\epsilon_s} [x - (W + x_n)]^2 + V_0, & W < x < W + x_n \\ V_0, & x > W + x_n \end{cases}
 \end{aligned}
 \quad \text{Equation 2}$$

where  $q$  is the electron charge,  $N_a$  is the acceptor concentration,  $N_d$  is the donor concentration,  $x_p$  and  $x_n$  are the boundaries of the space charge region in the  $p$ - and  $n$ -sides, respectively,  $L_b$  is the barrier length,  $L_w$  is the well width,  $W$  is the total length of the active region,  $l_w$  is the total length of the quantum wells for a distance lower than  $x$ ,

and  $V_0 = V_{bi} - V_a$ , where  $V_{bi}$  is the built-in voltage and  $V_a$  is the applied voltage. The  $x_n$  and  $x_p$  distances can be calculated from:

$$\text{Equation 3} \quad V_0 = \frac{qN_a}{\epsilon_s} x_p W + \frac{qN_a}{2\epsilon_s} x_p^2 + \frac{qN_d}{2\epsilon_s} x_n^2$$

$$N_a x_p = N_d x_n ,$$

taking into account charge neutrality. The potential calculated in this way allows us to obtain the band structure analytically, after adding the band-offsets at the InGaN-GaN interfaces.<sup>92</sup> The results for the conduction band diagram are shown in Figure 41 at different forward biases.

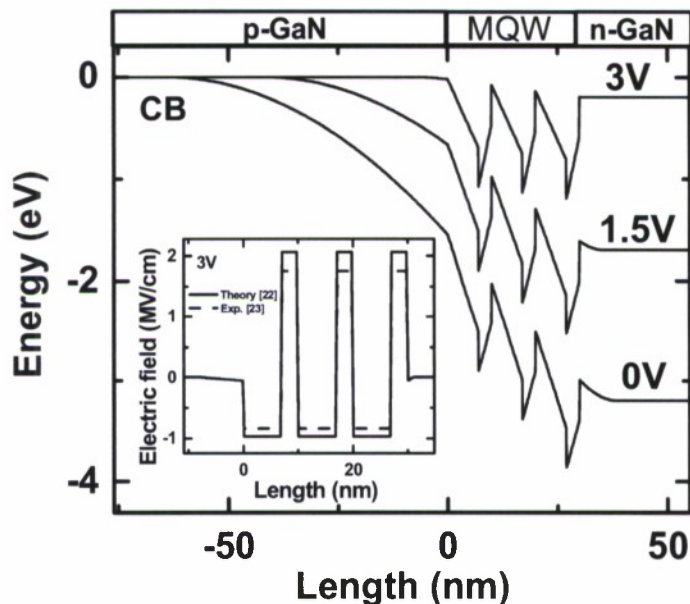


**Figure 41.** Conduction band (CB) diagram at 0, 1.5 and 3 V calculated from Equation 2. Inset: Electric fields calculated from the experimental and theoretical values for the piezoelectric constants.<sup>93,94</sup>

From the derivative of the potential, we can obtain the electric field distribution. The experimental values of the polarization in InGaN/GaN QWs found in the literature are slightly lower than the theoretical ones; in the inset of Figure 41, we compare the electric field strength provided by the experimental<sup>93</sup> and theoretical<sup>94</sup> piezoelectric constants, interpolating linearly to determine the InGaN constants in both cases. Using the theoretical values, electric field strengths of 1.4 MV/cm and 0.96 MV/cm are predicted in the barriers at 0 and 3.0 V, respectively. On the other hand, experimental values yielded electric fields of 1.2 MV/cm and 0.83 MV/cm at the same voltages. However, our analysis lacks the screening effect induced by the current flow and a self-consistent Poisson-Schrodinger calculation with time dependency would be needed to account for this. Although similar electric fields have been calculated in more accurate modeling by other authors,<sup>95,96,97</sup> the screening effects at those voltages and current levels cannot be completely neglected. Actually, a situation of negative average electric field (NAE) has

been predicted in Ref. [97] at forward biases just before the flat band condition, leading to consequent electron and hole accumulation at the edges of the quantum well region. This charge distribution is depicted in Figure 42, in which we have superimposed the potential created by a hypothetical dipole caused by the accumulation of electrons and holes in the first and last wells, respectively. We believe that this is likely to be the case in our devices at 3 V. The flat band condition will be reached at slightly higher voltages, when the charge accumulated at the edges redistributes uniformly in the three wells. This process may occur by thermionic emission or tunneling, and gives rise to the step-like feature found in the I-V characteristics. The observation of a similar feature in InGaN/GaN MQW Schottky barrier photodiodes with NAE seems to support this hypothesis.<sup>78,88</sup>

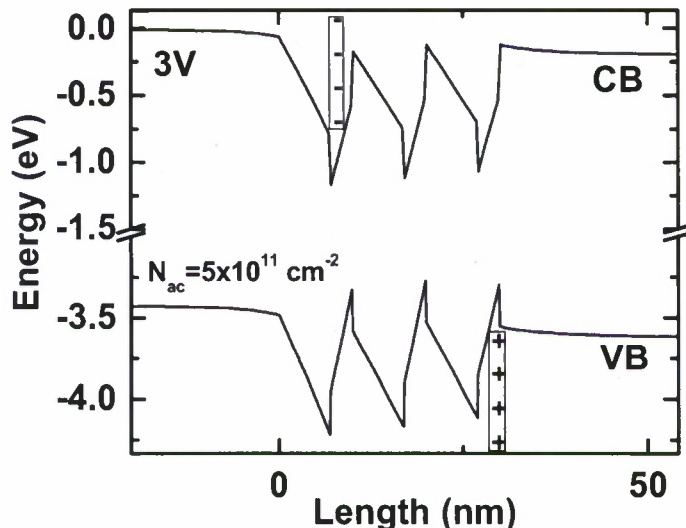


*Figure 42. Charge accumulation at the edges of the MQW region predicted by Ref. [26] under high injection conditions. The band diagram was calculated as the sum of (1) and the potential of the dipole when the accumulated charge is  $5 \times 10^{11} \text{ cm}^{-2}$  in the first (electrons) and last (holes) wells.*

### 6.3.3 Barrier electric field

From the previous discussion, it is expected that the strong electric fields in the barriers play an important role in the absorption close to the GaN bandgap. Binet et al. observed the effects of electric fields on Wannier excitons via transmission and photocurrent measurements.<sup>98</sup> However, they only experimented with fields ranging from 0 to 40 kV/cm.

To measure the effect under stronger electric fields, we used a *p-i-n* GaN structure with a 200 nm thick intrinsic region. Photocurrent and electro-absorption measurements were carried out at reverse bias voltages between 0 and -75 V (near breakdown voltage). Thus, electric fields up to 2 MV/cm were tested.

Photocurrent ( $I_{ph}$ ) measurements under back-illumination of the *p-i-n* diodes provided the spectra shown in Figure 43 as a function of bias. The increasing field in the intrinsic region results in a shift and broadening of the absorption cut-off. This behavior has been also found before in similar structures.<sup>99,100</sup> At low voltages, excitonic effects are likely to

dominate the absorption spectrum. However, at voltages near breakdown, excitonic absorption weakens and band-to-band transitions become dominant. The electric field strength in the intrinsic region was estimated from the data fitting of the photocurrent measurements using the absorption coefficient dependence on the electric field, and taking into account that the  $I_{ph} \propto \alpha$  approximation is reasonably valid when  $\alpha L_i \ll 1$ ,  $L_i$  being the thickness of the intrinsic region. Therefore, in the Wentzel-Kramers-Brillouin approximation, the photocurrent is given by<sup>101</sup>

$$\text{Equation 4} \quad I_{ph}(hv) \propto \exp \left[ -\frac{4\sqrt{2m_\mu}(E_{gap} - hv)^{3/2}}{3qF\hbar} \right]$$

where  $E_{gap}$  is the energy gap,  $hv$  is the photon energy,  $m_\mu$  is the reduced effective mass, and  $F$  is the electric field. The photocurrent curves are then fitted using Equation 4 to get the electric field strength.

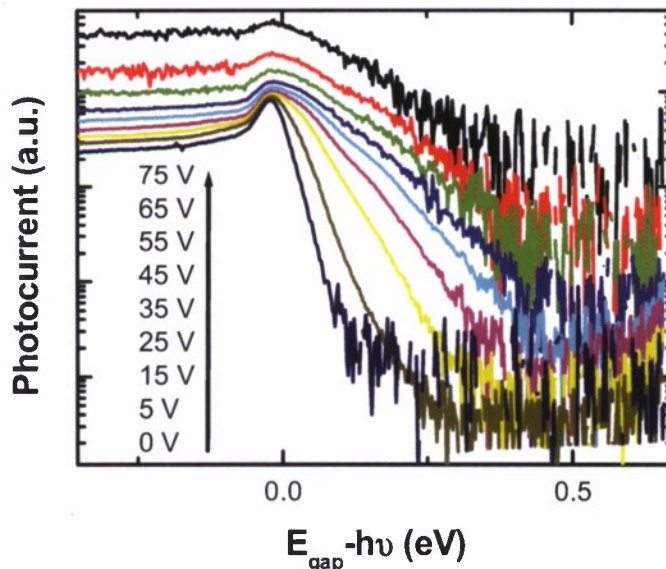


**Figure 43.** Photocurrent spectra measured as a function of reverse bias in p-i-n diodes with an intrinsic layer thickness of 200 nm.

The electro-absorption measurements, performed through the semitransparent top contact in the p-i-n diodes, allowed us to experimentally obtain the absorption coefficient at different reverse bias voltages and correlate these results with the electric field strengths obtained in photocurrent measurements (Figure 44). The inset of Figure 44 then shows the absorption coefficient dependence on the electric field. At wavelengths close to the band edge, the absorption coefficient follows a  $F^{-s}$  dependence with  $s < 1$ . This departure from theory may be caused by absorption in the p-GaN layer, which could enhance the absorption coefficient at wavelengths close to the band-edge, but would not have effect on the photocurrent, since this is the result of the absorption in the intrinsic region. As the wavelength increases, the  $s$  value approaches 1.

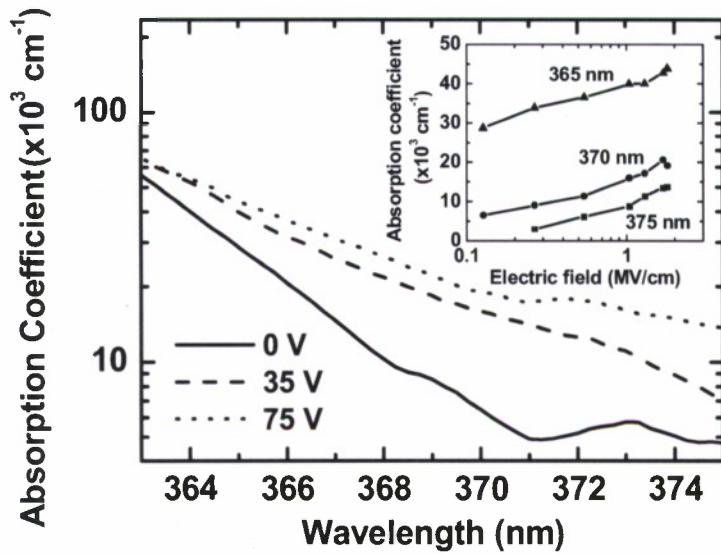


Figure 44. Absorption coefficient obtained as a function of wavelength in the p-i-n structures at different reverse voltages (0, 35, and 75 V). Inset: Absorption coefficient at 365, 370, and 375 nm as a function of the electric field.

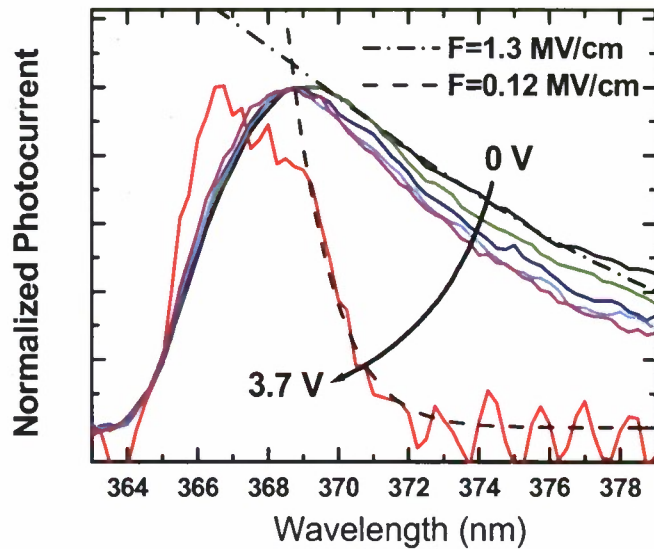


Figure 45. Photocurrent measurements in the p-MQW-n diodes at different forward biases ranging from 0 to 3.7 V. The dotted-dashed line represents the fitting to the photocurrent curve at 0 V using (3). The dashed line represents the fitting at 3.7 V. The electric field values obtained in each case are included.

From Equation 4, we can also obtain the electric field strength in the barrier of the  $p$ -MQW- $n$  diodes. Figure 45 depicts the result of this fitting at 0 and 3.7 V. In both cases, the response close to the lower cut-off wavelength is attributed to the GaN barrier, and it is assumed that the response from the InGaN wells remains beneath it. Thus, the average

electric fields obtained from the fitting are  $1.3 \pm 0.2$  MV/cm at 0 V and  $0.12 \pm 0.05$  MV/cm at 3.7 V. The first value is in fairly good agreement with the calculated values provided by Equation 2. The slope of the photocurrent measurements becomes more abrupt as the forward bias increases (Figure 45), making the calculated electric field decrease, as expected from the previous analysis. The value at 3.7 V represents a direct measurement of the barrier electric field under high carrier injection, which accounts for the screening effect. Consequently, it is significantly lower than the value predicted by the calculation. Therefore, photocurrent provides an excellent way of measuring the electric fields in the barriers, which are crucial elements in the inter-well transport.

#### 6.4 Model and I-V curve analysis

From the charge accumulation depicted in Figure 42, one can analyze the consequences of the barrier absorption. Carriers photogenerated in the barriers due to the Franz-Keldysh effect are going to be quickly separated and trapped in the adjacent wells. There, they form a dipole that screens the electric field in the barrier, enhancing the thermionic emission over the barrier and the tunneling current, resulting in a total current increase. This electric field opposes the electric field of the long-range potential created by the accumulated charge at the edges of the MQW region, and makes the band diagram approach a flat band situation: Figure 46 illustrates this process. The escape ( $\tau_{\text{esc}}$ ) and recombination ( $\tau_r$ ) times of electrons and holes will determine the lifetime ( $\tau$ ) of this dipole.

Once the flat band condition is reached, the charge distributes uniformly across the wells either by tunneling or by thermionic emission. The step-like feature is the result of this process, which is accompanied by a stronger luminescence due to the enhanced recombination rate. This behavior was also observed at 77 K, which suggests a dominant tunneling process less sensitive to thermal effects.

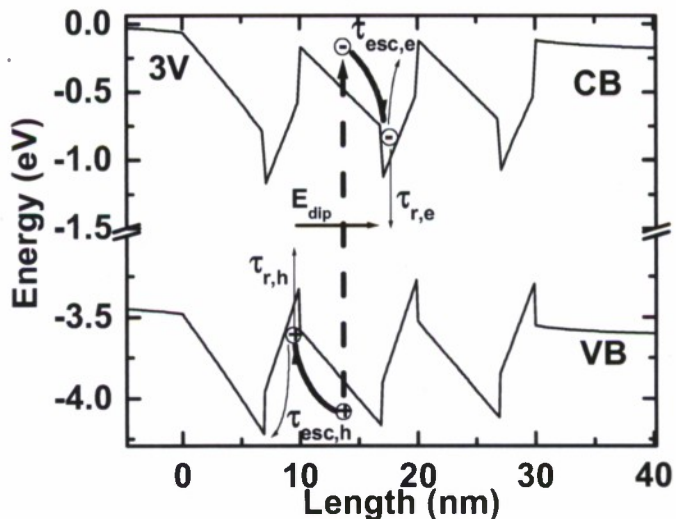


Figure 46. Scheme of the electron-hole pair generation in the barriers and relaxation to the adjacent wells.  $E_{\text{dip}}$  represents the created dipole, and  $\tau_{r,i}$  and  $\tau_{\text{esc},i}$  the recombination and escape times from the wells for electrons (e) and holes (h).

In order to gain insight into the conduction mechanisms, the I-V characteristics of standard *p-i-n* diodes and *p-MQW-n* diodes were compared (Figure 47). The thickness of the intrinsic region in the *p-i-n* diodes was equal to the total thickness of the active region in the *p-MQW-n* diodes. Two main differences are noticeable between both I-V characteristics. One is the right-shift of the *p-MQW-n* curve at low voltages; this shift is caused by the extra potential drop ( $\phi_{MQW}$ ) in the heterojunctions forming the MQW region, which is enhanced by the presence of piezoelectric fields.<sup>78</sup> The other difference is that the *p-i-n* diodes do not present the step-like feature, and in fact, no optical response was observed at that range of voltages (inset of Figure 47). This confirms that both phenomena are a direct consequence of the MQW.

The general model for the I-V characteristic in *p-i-n* diodes is given by

$$\text{Equation 5} \quad I = I_0 \exp[qV/\eta kT] \quad (\text{with } V > 3kT/q)$$

where  $I_0$  is the saturation current,  $k$  is the Boltzmann constant,  $T$  is the temperature and  $\eta$  is the ideality factor. We neglect the effect of the series resistance for the sake of clarity. Using this equation, an  $\eta = 3.7$  is obtained from the fitting of the *p-i-n* diodes at low voltages. This high ideality factor departs from the Sah-Noyce-Shockley theory, which is a common characteristic of nitride diodes.<sup>102</sup> A possible explanation might be a slight Schottky rectifying behavior of the *p-GaN* contact.

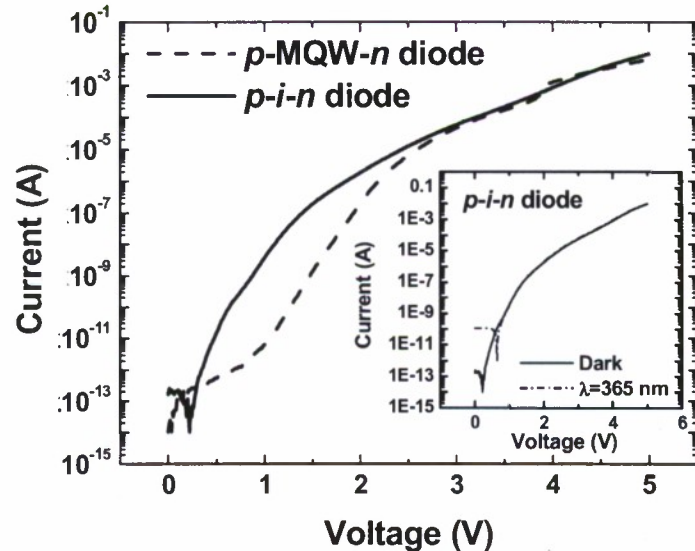


Figure 47. I-V characteristics obtained at forward bias from the *p-MQW-n* diodes under study and *p-i-n* diodes with an *i*-region thickness of 30 nm. Inset: I-V characteristics of the *p-i-n* diodes in darkness and under back-illumination at 365 nm.

From the I-V characteristics, the effect of the MQW can be taken into account including an extra potential drop term ( $\phi_{MQW}$ ). Therefore,

$$\text{Equation 6} \quad I = I_0 \exp[q(V - \phi_{MQW})/\eta kT]$$

The  $\phi_{MQW}$  obtained from the fitting of the  $p$ -MQW- $n$  sample at low voltages is 0.62 V, while the ideality factor is equal to 3.7, as in the  $p$ - $i$ - $n$  diode. At high voltages, the potential drop at the heterojunctions is reduced by two effects: the screening of the piezoelectric field caused by the injection of carriers and, under illumination, the screening caused by photogenerated carriers in the barrier, as described previously. Then, two terms can be added to account for both effects

$$\text{Equation 7} \quad \phi_{MQW} = \phi_0 - \phi_{inj}(I) - \phi_{ph}(P_{opt})$$

where  $\phi_{inj}$  and  $\phi_{ph}$  represent the lowering effect on the potential drop due to the current injection and optical power excitation ( $P_{opt}$ ), respectively. At low optical powers, we may consider as a first order approximation that  $\phi_{inj}(I_{dark}) \approx \phi_{inj}(I_{il})$ , which allows us to calculate the ratio between the current under illumination ( $I_{il}$ ) and in darkness ( $I_{dark}$ ) as

$$\text{Equation 8} \quad \frac{I_{il}}{I_{dark}} = \exp[q\phi_{ph}(P_{opt})/\eta kT]$$

The lowering effect on the barriers due to the optical power excitation can be written as

$$\text{Equation 9} \quad \phi_{ph}(P_{opt}) = \frac{P_{opt}\tau(1 - \exp(-\alpha n L_b))}{\epsilon_s A} n L_b$$

where  $\tau$  is the dipole lifetime,  $A$  the illuminated area,  $n$  is the number of barriers,  $\alpha$  is the absorption coefficient and  $L_b$  the barrier length. Hence, from Equation 8 and Equation 9, we can determine approximately the dipole lifetime needed to get the  $I_{il}/I_{dark}$  values measured in the samples under study. At 11 nW, this ratio was about 2 under uniform illumination across a 0.023 mm<sup>2</sup> area device. From Figure 45, an absorption coefficient of  $2.8 \times 10^4$  cm<sup>-1</sup> is expected for the electric field calculated in the barriers. These values yield a dipole lifetime of 0.01 s. On the other hand, the dipole lifetime is given by  $\tau^{-1} = 1/\tau_r + 1/\tau_{esc}$ . From the temporal response plot,  $\tau_r$  can be estimated to be a few seconds. Our model predicts almost three orders of magnitude lower dipole lifetime, which means that the carrier escape time from the wells may dominate the dipole quenching.

At low powers, Equation 8 can be approximated by

$$\text{Equation 10} \quad \frac{I_{il}}{I_{dark}} \approx 1 + q\phi_{ph}(P_{opt})/\eta kT$$

$$\text{Equation 11} \quad I_{ph} = \frac{I_{il} - I_{dark}}{I_{dark}} \approx q\phi_{ph}(P_{opt})/\eta kT$$

which accounts for the linear dependence of the photocurrent on incident power observed in our experiments for the gain band R1.

On the other hand, the R2 band is the result of the tunneling current prior to the flat-band condition. The electrons and holes accumulated at the edges of the active region under high carrier injection travel through the barriers to meet in the wells. The barrier illumination screens part of the potential at the heterointerfaces, which is enhanced by the polarization fields, and increases the tunneling probability. Thus, the transition from NAE to the flat-band condition takes place at slightly lower voltages (see inset Figure 36). The high current delivered makes this gain mechanism promising for high sensitivity detection.

## 6.5 Detection of low photon fluxes

We explore the use of this tunneling effect of band R2 to detect low photon fluxes. As concluded from the previous discussion, the illumination of the barriers helps to screen the long-range potential, reaching the flat-band condition at lower voltages. Biasing the device at a sub-threshold voltage, we make it ready to trigger the tunneling process in presence of light. The device is kept active for a short time, after which it is biased back to zero to sweep the charges from the wells and reduce the dipole lifetime. This operation mode is similar to the Geiger mode operation of avalanche photodiodes using a gated quenching circuit, but with a much lower baseline voltage.

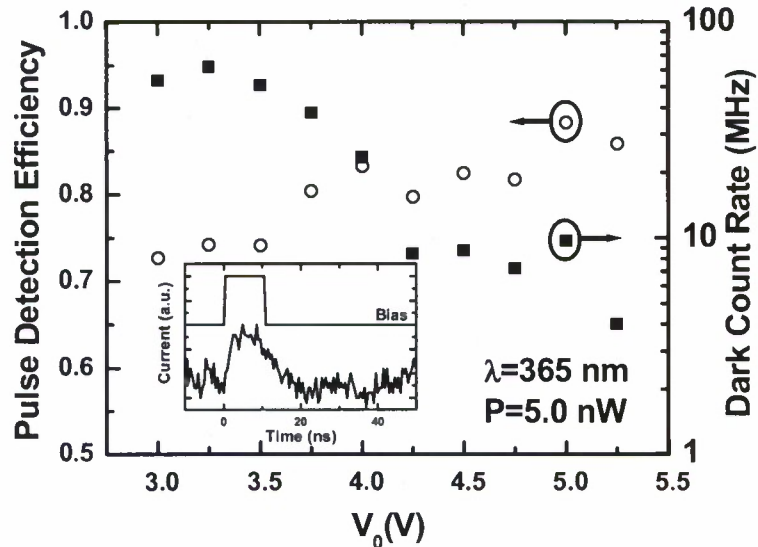


Figure 48. Left axis: Detection efficiency of 10 ns bias pulses with a  $V_0$  amplitude under illumination with 5.0 nW ( $\sim 90 \text{ ph/pulse}$ ). Right axis: Dark count rates. Inset: Bias pulse applied to the device for detection of low photon fluxes, and current pulse delivered under barrier illumination.

To test this procedure, the device was biased using a pulse of amplitude  $V_0 = 3 - 5.2 \text{ V}$  and width 10 ns at a repetition rate of 10 KHz. The device was biased to zero in between pulses. The cathode of the device was connected to the  $50 \Omega$  input of a pulse counter. An optical power of 5 nW at 365 nm was used to pump the diode, equivalent to

~90 ph/pulse. The inset of Figure 48 shows the photocurrent pulse obtained under back-illumination at 365 nm during the bias pulse. The pulse detection probability was measured as the number of detected pulses divided by the total number of bias pulses. The dark count rate is the probability of detecting a false count divided by our pulse width.

For the range of voltage amplitudes tested (3.00 – 5.25 V), the pulse detection probability increased slightly with bias as the dark count rate decreased. Around the voltage at which the step-like feature takes place, the dark count rate reduces an order of magnitude. The best values obtained are a pulse detection efficiency of about 85% and a dark count rate of 4 MHz, at a voltage amplitude of 5.25 V. Although, these values are still far from the current state-of-the-art of UV single-photon detectors based on APDs,<sup>102,80</sup> investigation of these devices is worthwhile since it may lead to revolutionary advantages such as lower bias voltages, larger active areas, or uniform response in the single-photon detection field.

## 6.6 Summary

High optical responses have been obtained under barrier illumination in forward biased *p*-InGaN/GaN MQW-*n* diodes. Two gain mechanisms are identified: the long-range inter-well potential screening (R1) and the tunnel effect through the barriers (R2). The absorption and photocurrent measurements allowed us to determine the effect of the piezoelectric field on the barrier absorption, within a good agreement with theoretical predictions. The I-V characteristics of our *p*-MQW-*n* have been modeled, corroborating the experimental findings. The capability of the tunnel effect to detect low photon fluxes has been demonstrated.

# 7 GaN Nanostructured *p-i-n* Photodiodes

## 7.1 Introduction

The use of nanostructures in traditional devices brings out new physics that can help to improve their performance up to unknown limits. New quantum and non-quantum effects arise when the dimensions of the devices are reduced to a nanometric scale. In nanopillars, quantum confinement effects in the lateral direction are only revealed when the lateral dimensions are lower than 50 nm.<sup>103</sup> For larger mesoscopic systems, quantum effects are not observable but the surface states also make their performance depart from that found in bulk-based devices.<sup>104,105</sup> In particular, light-matter interaction and carrier transport are severely affected in those systems.

The optimization of GaN *p-n* structures is important for the development of high quality ultraviolet (UV) photodiodes and light-emitting diodes. Anomalous ideality factors ( $n \gg 2$ ) have been reported in these structures and attributed to surface band bending underneath the *p*-type contact.<sup>106</sup> Furthermore, dead regions have been identified close to the *p*-GaN surface in *p-i-n* photodiodes due to this downward bending.<sup>107</sup> Recently, nanopatterned nitride samples have exhibited enhanced luminescence due to the extraction of guided modes from nanopillar arrays.<sup>108</sup> In this work, we present the fabrication of GaN nanostructured *p-i-n* photodiodes by e-beam lithography (Figure 49) and the comparison of their current-voltage (I-V) characteristics with bulk devices in darkness and under illumination.

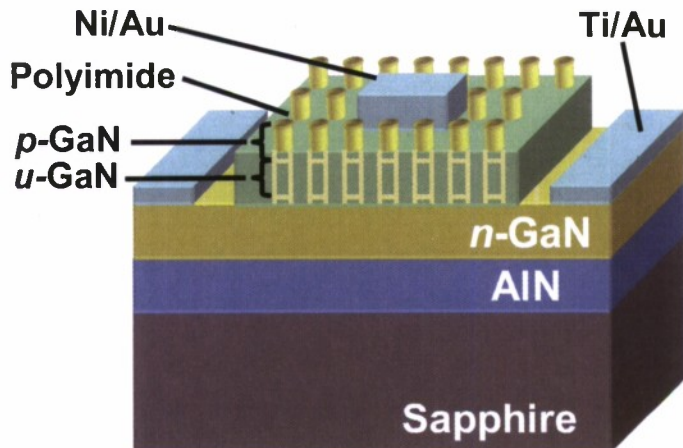


Figure 49. Schematic diagram of the device layout.

## 7.2 Material Growth & Processing

Samples were grown by metal-organic chemical-vapor deposition on transparent AlN templates on double side polished c-plane sapphire substrates for back-illumination. The structure consisted of a *p-i-n* GaN junction with carrier concentrations of  $(5 - 10) \times 10^{17} \text{ cm}^{-3}$  for the *p*-type GaN:Mg layer and  $(3 - 5) \times 10^{18} \text{ cm}^{-3}$  for the *n*-type GaN:Si layer; the *i* region was an undoped GaN layer with a residual carrier concentration in  $10^{16} \text{ cm}^{-3}$ . The thicknesses of the *p*-type, intrinsic, and *n*-type layers were 285, 200 and 200 nm, respectively.

A Ni/Au (30/30 Å) thin layer was deposited onto the *p*-type surface and annealed in air ambient at 500 °C for 10 min prior to nanopillar fabrication. For nanopillar fabrication, samples were coated with approximately 100 nm polymethylmethacrylate (PMMA) and soft baked. Lithography was performed using a Leica LV-1 electron beam system. A 6 mm × 4 mm dot field was patterned in the PMMA, with a step size of 1 μm. E-beam focus and dose were adjusted to obtain a dot size in the hundred nanometer range. After exposure, the resist was developed using a mixture of methylisobutylketone (MIBK) and isopropanol. A metal mask consisting of a 720 Å thick Ni layer was deposited using electron-beam evaporation and a lift-off procedure followed. Semiconductor etching was performed with a Plasmatherm SLR Series ECR-RIE system. The nanopillar structures were created using a SiCl<sub>4</sub>:Ar plasma etch process. The etch depth was about 520 nm and the resulting nanopillar diameter about 200 nm. The resulting packing density was about 0.01.

HD Microsystems polyimide was spin-applied to the sample and baked with a mean thickness of around 1.9 μm. The material filled the spaces between the nanopillar structures and served as an insulating layer between the top and bottom contacts. Oxygen plasma was used to remove the polyimide back. An scanning electron microscopy (SEM) image of the etched GaInAs/InP nanopillars after polyimide deposition and etching is shown in Figure 50. The etchback process revealed the top 100 nm of the nanopillars approximately. Standard lithography was then used to define circular contacts on the nanostructured surface with 625, 2025 and 3025 μm<sup>2</sup> areas; Ni/Au (400/1200 Å) top

contacts were formed by e-beam evaporation and subsequent lift-off. The rests of polyimide that surrounded these contacts were removed by using oxygen plasma, and followed by Ti/Au (400/1200 Å) bottom contact fabrication after standard lithography, e-beam evaporation and lift-off. Figure 49 illustrates the device scheme after processing. For comparison purposes, bulk devices were also fabricated on the same wafer, following the procedure described elsewhere.<sup>109</sup>

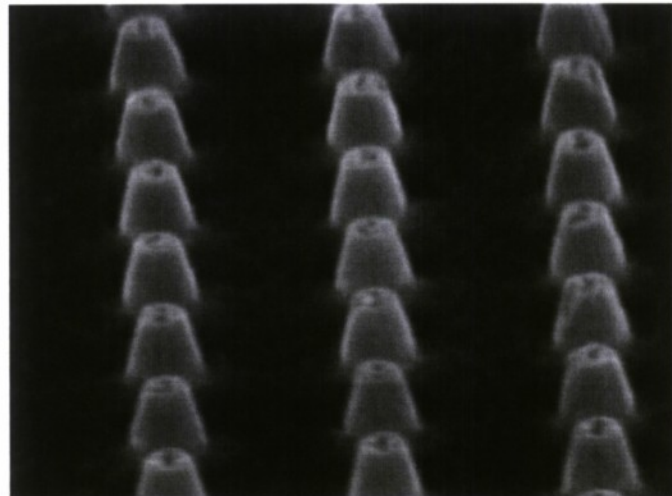


*Figure 50. SEM viewgraph of the nanopillar surface array after polyimide deposition and etch-back.*

### 7.3 Results and Analysis

I-V measurements were performed using a HP4155A curve tracer and a probe station. Ten devices were measured for each active area and their characteristics averaged. The resulting curves of the nanostructured diodes show strong rectifying behavior with about seven-order-of-magnitude contrast between the current levels at 5 V and -5 V (Figure 51). Unlike bulk diodes, which have currents under the noise floor of the system, increasing leakage currents with reverse bias are observed in the picoampere range. The undetectable current level observed in reference thin polyimide layers corroborates the good insulating properties of the polyimide and allows us to rule out the conduction through it as the dominant leakage source. On the other hand, the leakage current observed in *p-n* diodes at low voltages has been previously attributed to the damage induced by the dry etching on the sidewalls of the mesa structures.<sup>110</sup> We believe that this is the mechanism responsible of the leakage in the nanostructured devices. As these have a much larger perimeter-to-area ratio than bulk devices, the reverse bias current might be enhanced by the effect of the surface leakage through the nanopillar sidewalls.

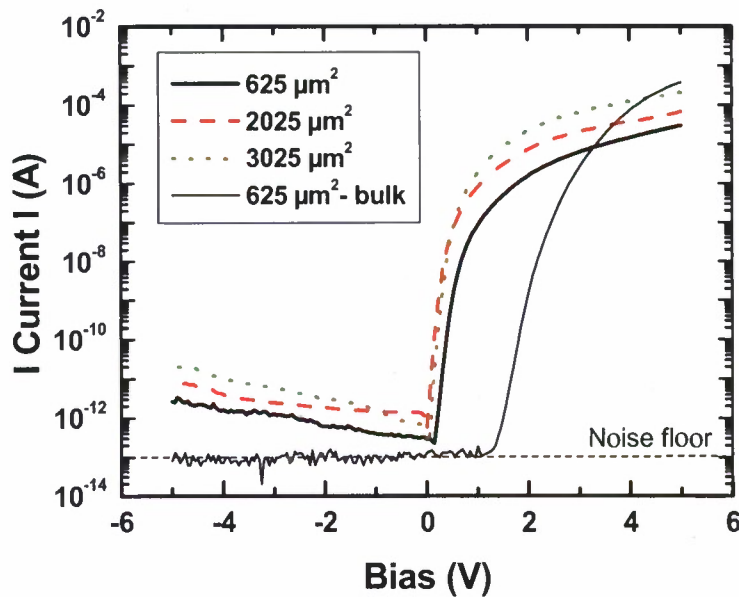


Figure 51. Current-voltage characteristics of GaN nanostructured p-i-n diodes with different device areas ( $625 \mu\text{m}^2$ ,  $2025 \mu\text{m}^2$  and  $3025 \mu\text{m}^2$ ) as compared to  $625 \mu\text{m}^2$  bulk diodes.

Taking into account that the separation between nanopillars is  $1 \mu\text{m}$ , the current per nanopillar can be calculated dividing the total current by the area of the device expressed in squared microns. Thus, the average leakage current per nanopillar obtained at  $-5 \text{ V}$  is  $5 \pm 2 \text{ fA}$  (Figure 52), which corresponds with a current density of  $0.16 \pm 0.06 \text{ A/m}^2$ .

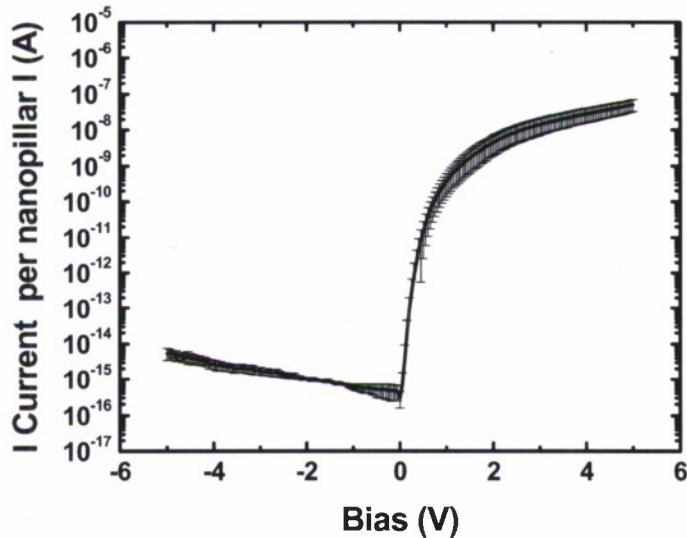


Figure 52. Average current-voltage characteristic per nanopillar.

It is also noticeable that a considerable reduction of the turn-on voltage in the nanostructured diodes takes place. Furthermore, the ideality factor obtained from the fitting of the I-V curves under low forward biases decreases from  $2.5 - 3.0$ , in the bulk diodes, to  $1.3 - 1.6$ , in the nanostructured diodes. The former are in good agreement with previous studies on GaN homojunction p-i-n diodes and have been attributed to the

downward band bending in the *p*-GaN surface.<sup>106,107</sup> However, the improvement of the ideality factor as well as the reduction of the turn-on voltage in the nanostructured devices are unexpected. As the top contact covers the surface of the nanopillar and part of the sidewall, a possible explanation is that this surface modification creates a new scenario for the *p*-contact formation. SiCl<sub>4</sub>-based etching increases the *n*-type character of the material near the surface.<sup>111</sup> A highly-doped thin layer formed in the sidewalls during etching could raise the hole tunneling current, minimizing the effect of the surface band bending. Moreover, the increase of the surface deep levels as a result of the etching could also benefit trap-assisted tunneling. In fact, Cl-based dry-etching recipes have demonstrated capabilities to alter the surface properties of GaN layers, improving the ohmicity of *p*-type contacts.<sup>112</sup> This reduction of the band bending effect would either contribute to lower the turn-on voltage of the diode.

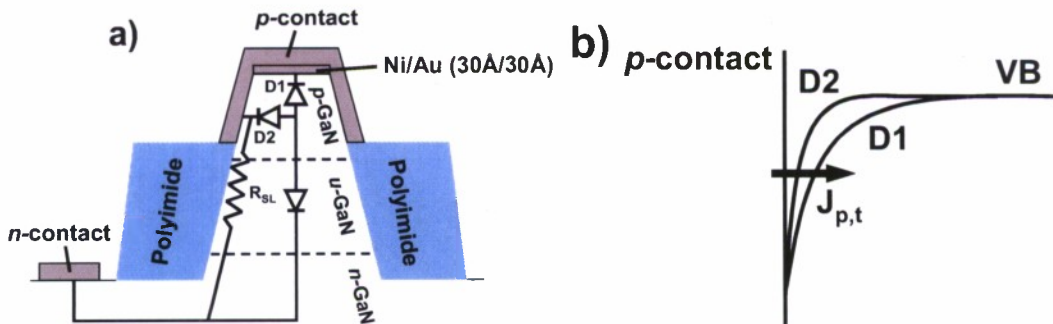


Figure 53. (a) Nanopillar cross-section and schematics of the proposed model. (b) Valence band-bending at the top (D1) surface of the nanopillar and sidewalls (D2) in the *p*-GaN region and tunneling mechanism ( $J_{p,t}$ ).

The proposed model is presented in Figure 53. The resistance  $R_{SL}$  represents the effect of the surface leakage, whereas D1 and D2 represent the metal-semiconductor barriers at the nanopillar top surface and sidewalls, respectively. The prominent band bending in D2 enhances tunneling, reducing the contact resistance and contributing to improve the ideality factor. However, these effects do not translate into more flowing current in the nanostructured devices under high forward biases ( $>3$  V) due to the lower conduction volume (packing density  $\ll 1$ ). Consequently, this current is very sensitive to the contact area, i.e. number of nanopillars under the contact (Figure 51(a)).

Photocurrent measurements under back-illumination were performed at 365 nm using a Xe lamp and a monochromator (Figure 54). In this configuration, the light is absorbed in the GaN after passing through the sapphire substrate and the AlN buffer layer with minimal losses. As shown in the inset of Figure 54, the optical response increased significantly with reverse bias: a quantum efficiency of 7% was calculated at 0 V, increasing up to 11.6% at  $-5$  V. On the other hand, the quantum efficiency of the bulk diodes was about 28% at 0 V, and increased up to 30% at 5 V. The increase in the bulk devices is attributed to the additional broadening of the depletion region. However, despite experiencing the same depletion region broadening, efficiency increases more than 1.5 times faster between 0 and  $-5$  V in nanostructured diodes than in bulk diodes.

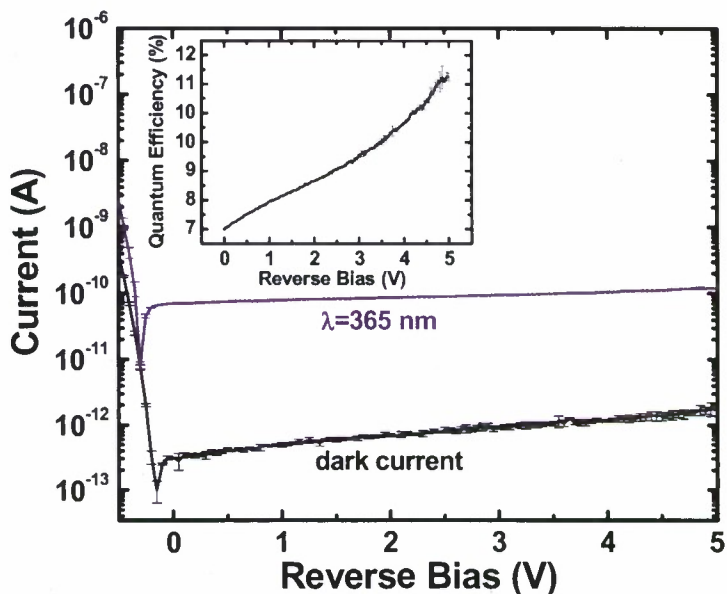


Figure 54. Reverse current of a  $625 \mu\text{m}^2$  diode in darkness and under illumination at  $365 \text{ nm}$ . Inset: calculated quantum efficiency as a function of bias.

Two loss mechanisms can account for the reduction of efficiency in nanostructured diodes: surface recombination and the existence of dead layers due to a low lateral collection efficiency of carriers into the nanopillar volume. The effect of surface recombination is difficult to predict, although it is reasonable to think that it should be fairly insensitive to the bias voltage. Thus, the faster increase of the photocurrent with bias in nanostructured devices compared to bulk diodes seems to confirm the lateral collection efficiency as a limiting factor. Therefore, we can expect a higher response from the reduction of the separation between nanopillars, which provides better lateral collection efficiency besides increasing the packing density. In fact, the distance between nanopillars is in our case about 800 nm, which is still slightly higher than most of the hole diffusion lengths reported in  $n$ -type GaN.<sup>113,114</sup> Moreover, the linear behavior of the optical response with the excitation power allows us to rule out other effects like photoconductive gain.

#### 7.4 Summary

In summary, the fabrication of GaN  $p-i-n$  photodiodes with embedded nanopillars is reported. Their I-V characteristics show an improvement of the quality factor compared to bulk diodes fabricated on the same material. The enhanced tunneling current through the  $p$ -type barrier contact is believed to be responsible of this behavior. Increasing quantum efficiencies with reverse bias were found due to the enhancement of the lateral collection efficiency.

### 8 Conclusions

We have investigated III-Nitride materials for the realization of novel optoelectronic devices. This has included: blue & green LEDs on LEO and conventional substrates,

InGaN quantum dot based LEDs, hybrid ZnO–InGaN based green LEDs, multi-quantum well detectors that show internal gain, and nano-structured UV detectors with improved electrical properties.

We have demonstrated super bright blue and green LEDs on both conventional substrates and lateral epitaxial overgrowth substrates. We have shown that by pulsing the precursors during InGaN growth, a better surface morphology can be achieved for the active layer. By using our new pulsed InGaN deposition, and temperature ramping technique, we have demonstrated high quality green LEDs. We have also investigated quantum dots for improved LED performance, however ultimately we found indium segregation to be a major limiting factor for improved device performance.

To avoid indium segregation we developed a novel approach of using ZnO in place of the standard GaN capping layer. This required inventing the structure due to the poor quality of existing *p*-type ZnO. The top layer was thus *n*-type ZnO rather than *p*-type GaN. Through the use of pulsed laser deposition (PLD) for the ZnO growth, the top layer growth step was performed at significantly lower growth temperature than is typically required for GaN growth in metalorganic chemical vapor deposition (MOCVD). In this way, thermally induced degradation of the InGaN active layers was combated. In our two years of developing this subject, we have extensively studied the fabrication and processing of hybrid devices in greater details their effects on the structural, electrical, and optical properties of hybrid LEDs.

We reported on the current-voltage (I-V) characteristic under forward biases obtained in low leakage, small size *p*-(In,Ga)N/GaN-*n* multi-quantum well diodes. Under barrier illumination, the devices present a high optical response with capabilities to detect optical powers in the pW range without further amplification. The band diagram was analyzed to gain insight on this phenomenon. We studied the effect that electric fields in the 1 MV/cm range have in the absorption edge of the GaN barriers. A model was proposed to account for the electro-optical characteristics observed. The detection of low photon fluxes was also reported under gated biasing.

We reported on the fabrication and current-voltage characteristics of nanostructured *p-i-n* photodiodes based on GaN. Each device comprises arrays of 1  $\mu$ m separated nanopillars fabricated by e-beam lithography with diameters of  $\sim$ 200 nm and heights of 520 nm. Strong rectifying behavior was obtained with an average reverse current per nanopillar of 5 fA at  $-5$  V. In contrast to GaN bulk *p-i-n* diodes, devices reproducibly show ideality factors lower than 2. Under back-illumination, the quantum efficiency increases significantly with reverse bias due to better lateral collection efficiency.

## 9 References

1. C. J. Humphreys, MRS Bulletin 33, **459** (2008).
2. N.F. Gardner, G.O. Muller, Y.C. Shen, G. Chen, S. Watanabe, W. Gotz, and M.R. Krames, Appl. Phys. Lett. **91**, 243506 (2007).
3. Y.H. Cho, S.K. Lee, H.S. Kwack, J.Y. Kim, K.S. Lim, H.M. Kim, T.W. Kang, S.N. Lee, M.S. Seon, O.H. Nam, and Y.J. Park, Appl. Phys. Lett. **83**, 2578 (2003).

---

4. I.K. Park, M.K. Kwon, J.O. Kim, S.B. Seo, J.Y. Kim, J.H. Lim, S.J. Park, and Y.S. Kim, *Appl. Phys. Lett.* **91**, 133105 (2007).
5. C. Bayram, F. H. Teherani, D. Rogers, and M. Razeghi, *Appl. Phys. Lett.* **93**, 081111 (2008).
6. Y. Narukawa, Y. Kawakami, M. Funato, S. Fujita, and S. Nakamura, *Appl. Phys. Lett.* **70**, 981 (1996).
7. M. Takeguchi, M.R. McCarty, and D. J. Smith, *Appl. Phys. Lett.* **84**, 2103 (2004).
8. S. J. Rosner, E.C. Carr, M.J. Ludowise, G. Girolami, and H.I. Erikson, *Appl. Phys. Lett.* **70**, 420 (1996).
9. S.F. Chichibu, H. Marchand, M.S. Minsky, S. Keller, P.T. Fini, J.P. Ibbetson, S.B. Fleischer, J.S. Speck, J.E. Bowers, E. Hu, U.K. Mishra, S.P. DenBaars, T. Deguchi, T. Sota, and S. Nakamura, *Appl. Phys. Lett.* **74**, 1460 (1999).
10. I. Ho and G.B. Stringfellow, *Appl. Phys. Lett.* **69**, 2701 (1996).
11. B. Van Daele, G. Van Tendeloo, K. Jacobs, I. Moerman, and M.R. Leys, *Appl. Phys. Lett.* **85**, 4379 (2004).
12. C. Wetzel, T. Salagaj, T. Detchprohm, P. Li, and J.S. Nelson, *Appl. Phys. Lett.* **85**, 866 (2004).
13. S. Nakamura, M. Senoh, N. Iwasa, and S. Nagahama, *Jpn. J. Appl. Phys.* **34**, L797-799 (1995).
14. S.J. Chang, W.C. Lai, Y.K. Su, J.F. Chen, C.H. Liu, and U.H. Liaw, *IEEE J. on Select. Top. On Quant. Elect.* **8**, 278 (2002).
15. Y.D. Qi, H. Liang, D. Wang, Z.D. Lu, W. Tang, and K.M. Lau, *Appl. Phys. Lett.* **86**, 101903 (2005).
16. T. Mukai, K. Takekawa, and S. Nakamura, *Jpn. J. Appl. Phys.* **27** L839-L841 (1998).
17. D.I. Florescu, V.M. Asnin, F.H. Pollak, A.M. Jones, J.C. Ramer, M.J. Schurman, and I. Ferguson, *Appl. Phys. Lett.* **77**, 1464 (2000).
18. P. Kozodoy, J.P. Ibbetson, M. Marchand, P.T. Fini, S. Keller, J.S. Speck, S.P. Denbaars, and U.K. Mishra, *Appl. Phys. Lett.* **73**, 975 (1998).
19. D.S. Li, H. Chen, H.B. Yu, H.Q. Jia, Q. Huang, and J.M. Zhou, *J. Appl. Phys.* **96**, 1111 (2004).
20. S. Tomya, T. Hino, S. Goto, M. Takeya, and M. Ikeda, *IEEE J Sel. Top. Quant. Elect.* **10**, 1277 Nov./Dec. (2004).
21. C. Bayram, J. L. Pau, R. McClintock, and M. Razeghi, *Applied Physics B* (accepted for publication) (2008).
22. S. Tomya, K. Funato, T. Asatsuma, T. Hino, S. Kijima, T. Asano, and M. Ikeda, *Appl. Phys. Lett.* **77**, 636 (2000).
23. A.E. Romanov, P. Fini, and J.S. Speck, *J. Appl. Phys.* **93**, 106 (2003).
24. H. Marchand, J.P. Ibbetson, P.T. Fini, S. Keller, S.P. DenBaars, J.S. Speck, and U.K. Mishra, *J. Cryst. Growth* **195**, 328 (1998).

---

25. D. Kapolnek, S. Keller, R. Vetry, R.D. Underwood, P. Kozodoy, S.P. Denbaars, U.K. Mishra, *Appl. Phys. Lett.* **71**, 1204 (1997).
26. H. Marchand, X.H. Wu, J.P. Ibbetson, P.T. Fini, P. Kozodoy, S. Keller, J.S. Speck, S.P. Denbaars, and U.K. Mishra, *Appl. Phys. Lett.* **73**, 747 (1998).
27. M. Takeya, K. Yanashima, T. Asano, T. Hino, S. Ikeda, K. Shibuya, S. Kijima, T. Tojou, S. Ansai, S. Uchida, Y. Yabuki, T. Aoki, T. Asatsuma, M. Ozawa, T. Kobayashi, E. Morita, and M. Ikeda, *J. Cryst. Growth* **221**, 646 (2000).
28. X. Xu, R.P. Vaudo, J. Flynn, and G.R. Brandes, *J. Electron. Mater.* **31**, 402 (2002).
29. A. Sakai, H. Sunakawa, and A. Usui, *Appl. Phys. Lett.* **73**, 481 (1998).
30. P. Fini, H. Marchand, J.P. Ibbetson, S.P. Denbaars, U.K. Mishra, and J.S. Speck, *J. Cryst. Growth* **209**, 581 (2000).
31. J.Z. Domagala, Z.R. Ztykiewicz, B. Beaumont, J. Kozlowski, R. Czernetzki, P. Prystawko, and M. Leszczynski, *J. Cryst. Growth* **245**, 37 (2002).
32. K. Hiramatsu, Y. Kawaguchi, M. Shimizu, N. Sawaki, T. Zheleva, R.F. Davis, H. Tsuda, W. Taki, N. Kuwano, and K. Oki, *MRS Internet J. Nitride Semicond. Res.* **2**, 6 (1997).
33. M.S. Ferdous, X. Wang, M. N. Fairchild, and S.D. Hersee, *Appl. Phys. Lett.* **91**, 231107 (2007).
34. D. V. Kuksenkov, H. Temkin, A. Osinsky, R. Gaska, and M.A Khan, *J. Appl. Phys.* **83**, 2142 (1998).
35. D. V. Kuksenkov, H. Temkin, A. Osinsky, R. Gaska, and M.A Khan, *Appl. Phys. Lett.* **72**, 1365 (1998).
36. J.W.P. Hsu, M.J. Manfra, D.V. Lang, S. Richter, S.N.G. Chu, A.M. Sergent, R.N. Kleiman, L.N. Pfeiffer, and R.J. Molnar, *Appl. Phys. Lett.* **78**, 1685 (2001).
37. Eric D. Jones. Light Emitting Diodes for General Illumination: Washington: OIDA, 2001.
38. Y. Cho, S.K. Lee, H.S. Kwack, J.Y. Kim, K.S. Lim, H.M. Kim, T.W. Kang, S.N. Lee, M.S. Seon, O.H. Nam, and Y.J. Park. *Appl. Phys. Lett.* **83**, (2003): 2578.
39. F.A. Ponce, S. Srinivasan, A. Bell, L. Geng, R. Liu, M. Stevens, J. Cai, H. Omiya, H. Marui, and S. Tanaka. *Phys. Stat. Sol.* **240**, (2003): 273.
40. T. Kozaki, H. Matsumura, Y. Sugimoto, S. Nagahama, and T. Mukai Proc. of SPIE **6133**, (2006): 613306.
41. M. Petro, A. Lorke, and A. Imomoglu. *Phys. Today* **54**, (2001): 46.
42. K. Tachibana, T. Someya, and Y. Arakawa. *Appl. Phys. Lett.* **74**, (1999): 383.
43. B. Damilano, N. Grandjean, S. Dalmasso, and J. Massies. *Appl. Phys. Lett.* **75**, (1999): 3751.
44. O. Moriwaki, T. Someya, K. Tachibana, S. Ishida, and Y. Arakawa. *Appl. Phys. Lett.* **76**, (2000): 2361. 38
45. Y. K. Su, S. J. Chang, L. W. Ji, C. S. Chang, L. W. Wu, W. C. Lai, T. H. Fang, and K. T. Lam. *Semicond. Sci. Technol.* **19**, (2004): 389.
46. S. Choi, J. Jang, S. Yi, J. Kim, and W. Jung. Proc. of SPIE **6479**, (2007): 64791F.

---

47. H. Zhou, S.J. Chua, K. Zang, L.S. Wang, S. Tripathy, N. Yakovlev, and O. Thomas, *Journal of Crystal Growth* **298**, (2007): 511.
48. Y. Wang, X.J. Pei, Z.G. Xing, L.W. Guo, H.Q. Jia, H. Chen, and J.M. Zhou, *J. Appl. Phys.* **101**, (2007): 033509.
49. V. Ranjan, G. Allan, C. Priester, and C. Delerue, *Phys. Rev. B* **68**, (2003): 115305.
50. N.F. Gardner, G.O. Muller, Y.C. Shen, G. Chen, S. Watanabe, W. Gotz, and M.R. Krames, *Appl. Phys. Lett.* **91**, 243506 (2007).
51. Y.H. Cho, S.K. Lee, H.S. Kwack, J.Y. Kim, K.S. Lim, H.M. Kim, T.W. Kang, S.N. Lee, M.S. Seon, O.H. Nam, and Y.J. Park, *Appl. Phys. Lett.* **83**, 2578 (2003).
52. I.K. Park, M.K. Kwon, J.O. Kim, S.B. Seo, J.Y. Kim, J.H. Lim, S.J. Park, and Y.S. Kim, *Appl. Phys. Lett.* **91**, 133105 (2007).
53. C. Bayram, J. L. Pau, R. McClintock, and M. Razeghi, "Comprehensive study of blue and green multi-quantum-well light emitting diodes grown on conventional and lateral epitaxial overgrowth GaN," *Applied Physics B* (DOI: 10.1007/s00340-008-3321-y).
54. I. Ho and G.B. Stringfellow, *Appl. Phys. Lett.* **69**, 2701 (1996).
55. B. Van Daele, G. Van Tendeloo, K. Jacobs, I. Moerman, and M. R. Leys, *Appl. Phys. Lett.* **85**, 4379 (2004).
56. D.J. Rogers, F.H. Teherani, A. Yasan, R. McClintock, K. Mayes, S.R. Darvish, P. Kung, M. Razeghi, and G. Garry, *Proc. SPIE* **5732** p. 412 (2005).
57. S.J. An, J.H. Chae, G.C. Yi, and G. H. Park, *Appl. Phys. Lett.* **92**, 121108 (2008).
58. Ya.I. Aliyov, J.E. Van Nostrand, and D.C. Look, *Appl. Phys. Lett.* **83**, 2943 (2003).
59. D.J. Rogers, F.H. Teherani, A. Yasan, K. Minder, P. Kung, and M. Razeghi, *Appl. Phys. Lett.* **88**, 141918 (2006).
60. D.J. Rogers, F.H. Teherani, P. Kung, K. Minder, and M. Razeghi, *Superlattice Microst.* **42**, p. 322-326 (2007).
61. C. Bayram, F. H. Teherani, D. Rogers, and M. Razeghi, *Applied Physics Letters*, **93**, 081111 (2008).
62. C. Bayram, J. L. Pau, R. McClintock, and M. Razeghi, *J. Appl. Phys.* **104**, 083512 (2008).
63. M. Smith, G. D. Chen, J. Y. Lin, H. X. Jiang, A. Salvador, B.N. Sverdlov, A. Botchkarev, H. Morkoc, and B. Goldenberg, *Appl. Phys. Lett.* **68**, 1883 (1996).
64. I. Adesida, A. Mahajan, E. Andideh, M. Asif Khan, D.T. Olsen, and J.N. Kuznia, *Appl. Phys. Lett.* **63**, 2777 (1993).
65. S.-W. Na, M. H. Shin, Y. M. Chung, J.G. Han, and N.-E. Lee, *J. Vac. Sci. Technol. A* **23**, 898 (2005).
66. J.-W. Bae, C.-H. Jeong, H.-K. Kim, K-K. Kim, N-G. Cho, T.-Y. Seong, S.-J. Park, I. Adesida, and G.-Y. Yeom, *Jpn. J. Appl. Phys.* **42**, L535 (2003).
67. W. Lim, L. Voss, R. Khanna, B.P. Gila, D.P. Norton, S.J. Pearson, and F. Ren, *Applied Surface Science* **253**, 889 (2006).

---

68. J.S. Park, H.J. Park, Y.B. Hahn, G.-C. Yi, and A. Yoshikawa, *J. Vac. Sci. Technol. B* **21**, 800 (2003).
69. C. Bayram, F. H. Teherani, D. Rogers, and M. Razeghi, *Appl. Phys. Lett.* **93**, 081111 (2008).
70. T. Takeuchi, C. Wetzel, S. Yamaguchi, H. Sakai, H. Amano, and I. Akasaki, *Appl. Phys. Lett.* **73**, 1691 (1998).
71. Y. D. Qi, H. Liang, D. Wang, Z. D. Lu, W. Tang, and K. M. Lau, *Appl. Phys. Lett.* **86**, 101903 (2005).
72. M. Asif Khan, J. N. Kuznia, D. T. Olson, J. M. Van Hove, M. Blasingame, and L. F. Reitz, "High-responsivity photoconductive ultraviolet sensors based on insulating single-crystal GaN epilayers," *Appl. Phys. Lett.*, vol. 60, pp. 2917-2919, Jun. 1992.
73. E. Muñoz, E. Monroy, J. A. Garrido, I. Izpura, F. J. Sanchez, M. A. Sanchez-Garcia, E. Calleja, B. Beaumont, and P. Gibart, "Photoconductor gain mechanisms in GaN ultraviolet detectors," *Appl. Phys. Lett.*, vol. 71, pp. 870-872, Aug. 1997.
74. F. Binet, J. Y. Duboz, E. Rosencher, F. Scholz, and V. Harle, "Mechanisms of recombination in GaN photodetectors," *Appl. Phys. Lett.*, vol. 69, pp. 1202-1204, Aug. 1996.
75. R. McClintock, J. L. Pau, K. Minder, C. Bayram, P. Kung, and M. Razeghi, "Hole-initiated multiplication in back-illuminated GaN avalanche photodiodes," *Appl. Phys. Lett.*, vol. 90, pp. 1411121-1411123, Apr. 2007.
76. J. B. Limb, D. Yoo, J. H. Ryou, W. Lee, S. C. Shen, R. D. Dupuis, M. L. Reed, C. J. Collins, M. Wraback, D. Hanser, E. Preble, N. M. Williams, and K. Evans, "GaN ultraviolet avalanche photodiodes with optical gain greater than 1000 grown on GaN substrates by metal-organic chemical vapor deposition," *Appl. Phys. Lett.*, vol. 89, pp. 0111121-0111123, Jul. 2006.
77. O. Katz, V. Garber, B. Meyler, G. Bahir, and J. Salzman, "Gain mechanism in GaN Schottky ultraviolet detectors," *Appl. Phys. Lett.*, vol. 79, pp. 1417-1419, Sep. 2001.
78. C. Rivera, J. L. Pau, and E. Muñoz, "Photocurrent gain mechanism in Schottky barrier photodiodes with negative average electric field," *Appl. Phys. Lett.*, vol. 89, pp. 2635051-2635053, Dec. 2006.
79. S. Verghese, K. A. McIntosh, R. J. Molnar, L. J. Mahoney, R. L. Aggarwal, M. W. Geis, K. M. Molvar, E. K. Duerr, and I. Melngailis, "GaN avalanche photodiodes operating in linear-gain mode and Geiger mode," *IEEE Trans. Electron Devices*, vol. 48, pp. 502-511, Mar. 2001.
80. J. L. Pau, R. McClintock, K. Minder, C. Bayram, P. Kung, M. Razeghi, E. Muñoz, and D. Silversmith, "Geiger-mode operation of back-illuminated GaN avalanche photodiodes," *Appl. Phys. Lett.*, vol. 91, pp. 0411041-0411043, Jul. 2007.

---

81. J. L. Pau, J. Anduaga, C. Rivera, A. Navarro, I. Alava, M. Redondo, and E. Muñoz, "Optical sensors based on III-nitride photodetectors for flame sensing and combustion monitoring" *Appl. Opt.*, vol. 45, pp. 7498-7503, Oct. 2006.
82. Y.-Z. Chiou, Y.-K. Su, S.-J. Chang, J. Gong, Y.-C. Lin, S.-H. Liu, and C.-S. Chang, "High detectivity InGaN-GaN multiquantum well p-n junction diodes," *IEEE J. Quantum Electron.*, vol. 39, pp. 681-685, May 2003.
83. A. Hangleiter, F. Hitzel, S. Lahmann, and U. Rossow, "Composition dependence of polarization fields in GaInN/GaN quantum wells," *Appl. Phys. Lett.*, vol. 83, pp. 1169-1171, Aug. 2003.
84. A. N. Cartwright, P. M. Sweeney, T. Prunty, D. P. Bour, and M. Kneissl, "Electric field distribution in strained p-i-n GaN/InGaN multiple quantum well structures," *MRS Internet J. Nitride Semicond. Res.*, vol. 4, 12, 1999.
85. H. Kollmer, J. S. Im, S. Heppel, J. Off, F. Scholz, and A. Hangleiter, "Intra- and interwell transitions in GaInN/GaN multiple quantum wells with built-in piezoelectric fields," *Appl. Phys. Lett.*, vol. 74, pp. 82-84, Jan. 1999.
86. M. Razeghi, P. Kung, D. Walker, M. Hamilton, and J. Diaz, "High quality LEO growth and characterization of GaN films on  $\text{Al}_2\text{O}_3$  and Si substrates," *Proc. SPIE*, vol. 3725, pp. 14-20, Apr. 1999.
87. C. Rivera, J. L. Pau, A. Navarro, and E. Muñoz, "Photoresponse of (In,Ga)N-GaN multiple-quantum-well structures in the visible and UVA ranges," *IEEE J. Quantum Electron.*, vol. 42, pp. 51-58, Jan. 2006.
88. C. Rivera, J. L. Pau, J. Pereiro, and E. Muñoz, "Properties of Schottky barrier photodiodes based on InGaN/GaN MQW structures," *Superlattices Microstruct.*, vol. 36, pp. 849-857, Oct.-Dec. 2004.
89. J. L. Pau, C. Rivera, J. Pereiro, E. Muñoz, E. Calleja, U. Schühle, E. Frayssinet, B. Beaumont, J. P. Faurie, and P. Gibart, "Nitride-based photodetectors: from visible to x-ray monitoring," *Superlattices Microstruct.*, vol. 36, pp. 807-814, Oct.-Dec. 2004.
90. S. M. Sze and K. K. Ng, *Physics of Semiconductor Devices*. New Jersey: John Wiley & Sons, 2007, ch. 2.
91. A. Bykhovski, B. Gelmont, and M. Shur, "The influence of the strain-induced electric field on the charge distribution in GaN-AlN-GaN structure," *J. Appl. Phys.*, vol. 74, pp. 6734-6739, Dec. 1993.
92. H. Zhang, E. J. Miller, E. T. Yu, C. Poblenz, and J. S. Speck, "Measurement of polarization charge and conduction-band offset at  $\text{In}_x\text{Ga}_{1-x}\text{N}/\text{GaN}$  heterojunction interfaces," *Appl. Phys. Lett.*, vol. 84, pp. 4644-4646, Jun. 2004.
93. A. Hangleiter, F. Hitzel, S. Lahmann, and U. Rossow, "Composition dependence of polarization fields in GaInN/GaN quantum wells," *Appl. Phys. Lett.*, vol. 83, pp. 1169-1171, Aug. 2003.
94. F. Bernardini, V. Fiorentini, D. Vanderbilt, "Spontaneous polarization and piezoelectric constants of III-V nitrides," *Phys. Rev. B*, vol. 56, pp. R10 024- R10 027, Oct. 1997.

---

95. U. M. E. Christmas, A. D. Andreev, and D. A. Faux, "Calculation of electric field and optical transitions in InGaN/GaN quantum wells," *J. Appl. Phys.*, vol. 98, pp. 0735221-0735223, Oct. 2005.
96. D. Oriato, and A. B. Walker, "Effects of piezoelectric field, bias and indium fluctuations on a InGaN-GaN single quantum well system," *Physica B*, vol. 314, pp. 59-62, Mar. 2002.
97. H. Wenzel, "Accurate modeling of InGaN quantum wells," *Opt. Quantum Electron.*, vol. 38, pp. 953-961, Sep. 2006.
98. F. Binet, J. Y. Duboz, E. Rosencher, F. Scholz, and V. Härle, "Electric field effects on excitons in gallium nitride," *Phys. Rev. B*, vol. 54, pp. 8116-8121, Sep. 1996.
99. K. A. McIntosh, R. J. Molnar, L. J. Mahoney, A. Lightfoot, M. W. Geis, K. M. Molvar, I. Meingailis, R. L. Aggarwal, W. D. Goodhue, S. S. Choi, D. L. Spcars, and S. Verghese, "GaN avalanche photodiodes grown by hybride vapor-phase epitaxy," *Appl. Phys. Lett.*, vol. 75, pp. 3485-3487, Nov. 1999.
100. K. Minder, J. L. Pau, R. McClintock, P. Kung, C. Bayram, and M. Razeghi, "Sealing in back-illuminated GaN avalanche photodiodes," *Appl. Phys. Lett.*, vol. 91, pp. 073513-1, Aug. 2007.
101. P. Baumgartner, C. Engel, G. Böhm, and G. Abstreiter, "Franz-Keldysh effect in lateral GaAs/AlGaAs based npn structures," *Appl. Phys. Lett.*, vol. 70, pp. 2876-2878, May 1997.
102. J. M. Shah, Y.-L. Li, Th. Gessmann, and E. F. Schubert, "Experimental analysis and theoretical model for anomalously high ideality factors ( $n >> 2.0$ ) in AlGaN/GaN p-n junction diodes," *J. Appl. Phys.*, vol. 94, pp. 2627-2630, Aug. 2003.
103. A. Gin, B. Movaghar, M. Razeghi, and G. J. Brown, *Nanotechnology* 16, 1814 (2005).
104. N. Malkova and C. Z. Ning, *Phys. Rev. B* 74, 155308 (2006).
105. Z.-M. Liao, K.-J. Liu, J.-M. Zhang, J. Xu, and D.-P. Yu, *Phys. Lett. A* 367, 207 (2007).
106. J. M. Shah, Y.-L. Li, Th. Gessmann, and E. F. Schubert, *J. Appl. Phys.* 94, 2627 (2003).
107. T. Li, J. C. Carrano, J. C. Campbell, M. Schurman, and I. Ferguson, *IEEE J. Quantum Electron.* 35, 1203 (1999).
108. S. Keller, C. Schaakc, N. A. Fichtenbaum, C. J. Neufeld, Y. Wu, K. McGroddy, A. David, S. P. DenBaars, C. Weisbuch, J. S. Speck, and U. K. Mishra, *J. Appl. Phys.* 100, 054314 (2006).
109. J. L. Pau, R. McClintock, K. Minder, C. Bayram, P. Kung, and M. Razeghi, *Appl. Phys. Lett.* 91, 041104 (2007).
110. C. Pernot, A. Hirano, H. Amano, and I. Akasaki, *Jpn. J. Appl. Phys.* 37, L1202 (1998).
111. A. T. Ping, Q. Chen, J. W. Yang, M. Asif Khan, and I. Adesida, *J. Electron. Mater.* 27, 261 (1998).

---

- 112. H. W. Choi, S. J. Chua, and X. J. Kang, *Phys. Stat. Sol. (a)* 188, 399 (2001).
- 113. R. J. Kaplar, S. R. Kurtz, and D. D. Koleske, *Appl. Phys. Lett.* 85, 5436 (2004).
- 114. K. Kamakura, T. Makimoto, N. Kobayashi, T. Hashizume, T. Fukui, and H. Hasegawa, *Appl. Phys. Lett.* 86, 052105 (2005).